DivIVA controls the dynamics of septum splitting and cell elongation in Streptococcus pneumoniae

Jennyfer Trouve, André Zapun, Laure Bellard, Dimitri Juillot, Anaïs Pelletier, Céline Freton, Morgane Baudoin, Rut Carballido-Lopez, Nathalie Campo, Yung-Sing Wong, et al.

AMERICAN SOCIETY FOR MICROBIOLOGY | mBio

Check for updates

| Molecular and Cellular Biology | Research Article

DivIVA controls the dynamics of septum splitting and cell elongation in *Streptococcus pneumoniae*

Jennyfer Trouve,[1] André Zapun,[1] Laure Bellard,[1] Dimitri Juillot,[2] Anais Pelletier,[3] Celine Freton,[3] Morgane Baudoin,[4] Rut Carballido-Lopez,[2] Nathalie Campo,[5,6] Yung-Sing Wong,[4] Christophe Grangeasse,[3] Cecile Morlot[1]

AUTHOR AFFILIATIONS See affiliation list on p. 22.

ABSTRACT Bacterial shape and division rely on the dynamics of cell wall assembly, which involves regulated synthesis and cleavage of the peptidoglycan. In ovococci, these processes are coordinated within an annular mid-cell region with nanometric dimensions. More precisely, the cross-wall synthesized by the divisome is split to generate a lateral wall, whose expansion is insured by the insertion of the so-called peripheral peptidoglycan by the elongasome. Septum cleavage and peripheral peptidoglycan synthesis are, thus, crucial remodeling events for ovococcal cell division and elongation. The structural DivIVA protein has long been known as a major regulator of these processes, but its mode of action remains unknown. Here, we integrate click chemistry-based peptidoglycan labeling, direct stochastic optical reconstruction microscopy, and *in silico* modeling, as well as epifluorescence and stimulated emission depletion microscopy to investigate the role of DivIVA in *Streptococcus pneumoniae* cell morphogenesis. Our work reveals two distinct phases of peptidoglycan remodeling during the cell cycle that are differentially controlled by DivIVA. In particular, we show that DivIVA ensures homogeneous septum cleavage and peripheral peptidoglycan synthesis around the division site and their maintenance throughout the cell cycle. Our data additionally suggest that DivIVA impacts the contribution of the elongasome and class A penicillin-binding proteins to cell elongation. We also report the position of DivIVA on either side of the septum, consistent with its known affinity for negatively curved membranes. Finally, we take the opportunity provided by these new observations to propose hypotheses for the mechanism of action of this key morphogenetic protein.

IMPORTANCE This study sheds light on fundamental processes governing bacterial growth and division, using integrated click chemistry, advanced microscopy, and computational modeling approaches. It addresses cell wall synthesis mechanisms in the opportunistic human pathogen *Streptococcus pneumoniae*, responsible for a range of illnesses (otitis, pneumonia, meningitis, septicemia) and for one million deaths every year worldwide. This bacterium belongs to the morphological group of ovococci, which includes many streptococcal and enterococcal pathogens. In this study, we have dissected the function of DivIVA, which is a structural protein involved in cell division, morphogenesis, and chromosome partitioning in Gram-positive bacteria. This work unveils the role of DivIVA in the orchestration of cell division and elongation along the pneumococcal cell cycle. It not only enhances our understanding of how ovoid bacteria proliferate but also offers the opportunity to consider how DivIVA might serve as a scaffold and sensor for particular membrane regions, thereby participating in various cell cycle processes.

KEYWORDS cell morphogenesis, cell division, cell elongation, peptidoglycan, cell wall, DivIVA, *Streptococcus pneumoniae*, ovococci, click chemistry, super-resolution microscopy, dSTORM, stimulated-emission-depletion microscopy

Invited Editor Kumaran S. Ramamurthi, Fred Hutchinson Cancer Center, Seattle, Washington, USA

Editor Nina R. Salama, Fred Hutchinson Cancer Center, Seattle, Washington, USA

Address correspondence to Cecile Morlot, cecile.morlot@ibs.fr.

The authors declare no conflict of interest.

See the funding table on p. 22.

Received 8 May 2024
Accepted 23 August 2024
Published 17 September 2024

Peptidoglycan (PG) is a three-dimensional network made of repeated *N*-acetylglucosamine-*N*-acetylmuramic acid disaccharide units cross-linked by short peptides (1). PG confers resistance to turgor pressure and a specific cellular shape that is adapted to the environment of the bacterium. This shape is tuned by the dynamics of PG synthesis and remodeling (2, 3), whose enzymatic actors are well known but whose organizational and regulatory factors remain poorly understood.

Assembly of the PG at the cell surface is performed by transglycosylase activities, which polymerize the PG precursor unit lipid II (a membrane-anchored disaccharide pentapeptide) into glycan chains, and by transpeptidase activities, which crosslink the peptide chains. PG synthases include SEDS proteins (Shape, Elongation, Division, and Sporulation), which carry transglycosylase activities, and Penicillin-Binding Proteins (PBPs) (4, 5). Class A PBPs (called aPBPs henceforth) are bifunctional enzymes carrying both transglycosylase and transpeptidase domains, while class B PBPs (bPBPs) are monofunctional transpeptidases (4, 5). bPBPs work in tandem with a cognate SEDS protein and participate in the cell division or cell elongation complexes known as the divisome and the elongasome, respectively (6–10). aPBPs work independently from these two machineries, presumably filling in gaps and/or densifying the PG mesh (11–13). PG remodeling, on the other hand, involves hydrolytic activities that cleave specific bonds within the nascent PG, allowing for example daughter cell separation or insertion of new material into the PG network (14).

In this work, we investigated PG synthesis and remodeling in the opportunistic human pathogen *Streptococcus pneumonia*e. This bacterium belongs to the morphological group of ovococci (e.g., streptococci and enterococci), whose shape results from septal and peripheral PG syntheses, which, respectively, allow cell division and cell elongation (15, 16). In *S. pneumoniae*, the divisome and elongasome contain the bPBP2x/FtsW and bPBP2b/RodA pairs, respectively (10, 15, 17–19). None of the three pneumococcal aPBPs (aPBP1a, aPBP2a, and aPBP1b) is essential, but inactivation of both aPBP1a and aPBP2a is lethal (20). Furthermore, aPBP1a modifies septal PG synthesized by the PBP2x/FtsW divisome pair (21). PG hydrolases related to cell division include the amidase/endopeptidase PcsB, the glucosaminidase LytB, and the muramidase Pmp23/MpgB (22–27). On the other hand, the muramidase MltG/MpgA works in conjunction with the elongasome (28).

Because PG synthetic and hydrolytic activities happen in regions with nanometer-scale dimensions, investigating their dynamics requires super-resolution microscopy methods that break the light diffraction barrier (29). Recently, the combination of click-chemistry bio-orthogonal labeling with dSTORM (direct Stochastic Optical Reconstruction Microscopy) and *in silico* modeling improved our understanding of cell morphogenesis in the ovoid-shaped bacterium *S. pneumoniae* (3, 30). Proteins responsible for septal and peripheral PG synthesis are recruited to mid-cell by the cytoskeletal protein FtsZ at the beginning of the cell cycle, and their activities are first confounded within an annular region whose nanometric dimensions approximate those of the ring formed by FtsZ (3, 31). Later on, two concentric synthesis regions progressively separate, with the inner region corresponding to septal PG synthesis and the outer region to peripheral PG (Fig. S1A) (3, 32). Importantly for this work, the study of PG dynamics by dSTORM brought support to a mechanism in which PG synthesis by the divisome at the membrane invagination front forms a septal matrix, which is then split at its edge by hydrolases to form the new cell hemispheres. Peripheral PG is inserted by the elongasome at the periphery of the septum, into freshly cleaved septal material or concomitantly with the cleavage (Fig. S1A) (3). In this model, septum remodeling through cleavage and incorporation of peripheral PG would, thus, be a key event allowing both cell separation and cell elongation. Because they modify septal PG, aPBPs probably also influence septum cleavage and/or peripheral PG insertion (21).

With regard to the mechanisms of septum remodeling, the membrane-associated coiled-coil protein DivIVA is thought to be a main player (33, 34). In *S. pneumoniae*, DivIVA is found at the division site and the cell poles, and it interacts with many elongation and

division proteins, including bPBP2x, bPBP2b, and aPBP1a (19, 33, 35, 36). The deletion of the *divIVA* gene results in chains of short pneumococcal cells, indicative of impaired cell separation and elongation (19, 36, 37). In *Streptococcus suis*, DivIVA interacts with MltG/MpgA, and its absence causes a cell elongation defect (38). Altogether, these observations point to a functional link between DivIVA and cell growth, but its exact function remains unknown.

Here, we used state-of-the-art fluorescence microscopy methods to investigate the role of DivIVA in *S. pneumoniae* cell morphogenesis. Using conventional epifluorescence microscopy and STED (stimulated-emission-depletion) microscopy, we describe the localization of DivIVA on either side of the division site. Importantly, by combining bio-orthogonal PG labeling, dSTORM imaging, and *in silico* modeling to analyze PG synthesis in *divIVA* mutants, we reveal that the dynamics of septum remodeling displays two phases along the pneumococcal cell cycle. During these two phases, DivIVA promotes both splitting of the septum and peripheral PG synthesis, ensuring that these two activities are synchronous around the septal periphery and consistently maintained all along the division cycle.

RESULTS

DivIVA localizes as a double ring at constricting division sites

Several studies have shown that DivIVA localizes at the division site in various bacterial species and, in some cases, at the cell poles, including in *S. pneumoniae* (35, 36, 39–41). To further document the localization of the pneumococcal DivIVA, we constructed a DivIVA-HaloTag (DivIVA-HT) fusion at the endogenous *divIVA* locus. This construct contains the full-length sequence of DivIVA, a 12 amino-acid linker (SGSGGEAAAKAG), and the HaloTag sequence (17, 42, 43). The comparable cell length and cell width distribution between the wild-type (WT) *S. pneumoniae* strain and cells expressing DivIVA-HT indicates that the fusion protein is functional (Fig. S2). Observation of DivIVA-HT using conventional fluorescence microscopy confirmed its septal and polar localization (Fig. 1A). Interestingly, it also showed an enrichment of the protein at mid- and late-division sites (constricting sites) compared with early-division sites (non-constricted sites) and cell poles (Fig. 1B), suggesting that the accumulation of DivIVA at mid-cell is correlated with division stages during which the septum is being remodeled (3). Moreover, the quantification of the fluorescent signal at division sites and cell poles showed that the amount of septal DivIVA increases as the amount of polar DivIVA decreases over time (Fig. 1C).

STED microscopy further revealed the localization of DivIVA as a double band at mid-cell (Fig. 1C and D) similar to its localization in *B. subtilis* (39, 44, 45). In *S. pneumoniae*, the double DivIVA bands, which correspond to the 2D projection of rings, are separated by a median distance of 93 ± 13 nm (n = 14).

DivIVA affects the dynamics of the pneumococcal cell cycle

In the absence of DivIVA, *S. pneumoniae* cells are still able to form complete septa, but they do not cleave them efficiently, forming chains of more than 70 µm (Fig. 2A) (19, 35, 36). To further characterize these defects, we analyzed the Δ*divIVA* strain by dSTORM following a short labeling pulse with the azido-D-Ala-D-Ala (aDA-DA) probe, which is incorporated into the growing PG (3, 30). The labeled cell chains display band-like patterns that result from the 2D projection of annular PG synthesis regions. The length of the labeled bands, therefore, measures the outer diameter of the pulse-labeled synthesis rings. Since they do not separate, the cells of the Δ*divIVA* strain could not be classified along the cell cycle as routinely performed with the WT strain (Fig. S1B) (3). Instead, we sought to classify the labeled PG synthesis sites. We observed an alternation of constricted and non-constricted labeling bands of various intensities (Fig. 2A). Interpreting the parental relationships between bands was complicated by the fact that a given site is not necessarily surrounded by sites of a single generation as in the WT strain (Fig. S1C) but

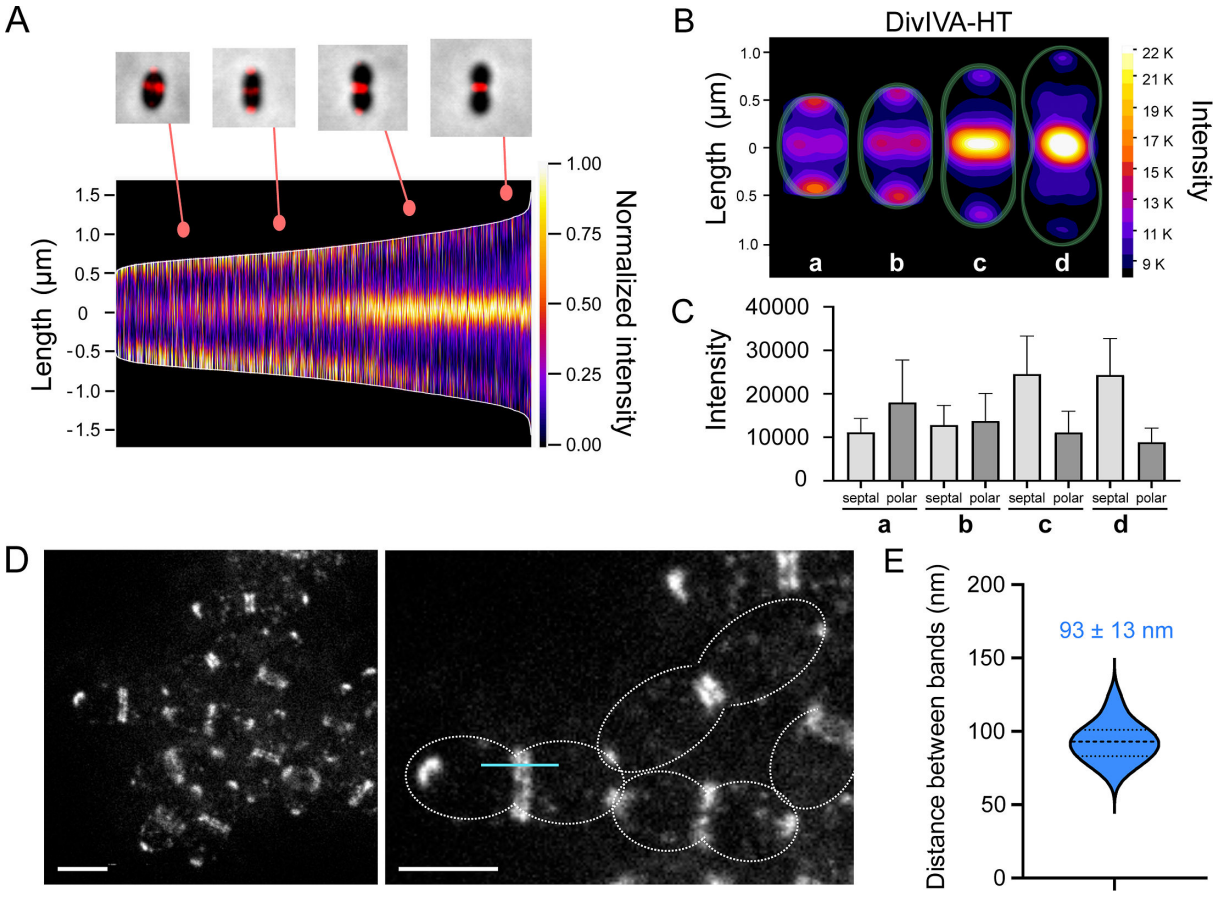

FIG 1 DivIVA localization in *S. pneumoniae*. Cells in the exponential growth phase were incubated with HT-JFX646 ligand before fluorescence microcopy. (A) Demograph showing the fluorescence intensity and diffraction-limited localization pattern of a DivIVA-HT fusion imaged by epifluorescence microscopy in 2,510 cells arranged according to their length. (B) Heatmaps built from the localization patterns shown in (A) (n = 2,510), representing the average DivIVA-HT fluorescence intensity and localization in groups of cells a to d, corresponding to four main stages of the cell cycle. Representative data are shown from two independent biological replicates. (C) Quantification of the average fluorescence intensity of DivIVA-HT at the septum and at the cell poles in groups of cells a to d (n = 112), corresponding to the four main stages of the cell cycle shown in (B). (D) STED images showing the localization of DivIVA-HT as polar foci or as two bands flanking the division site. The right panel is a zoom-in of the left panel. On the right panel, the cell contour is delineated with a dashed line, and the blue line indicates a typical region used to generate intensity plot profiles. Scale bars, 1 µm. (E) Violin plot showing the distribution of the distances separating DivIVA bands at midcell. The thin and thick dashed horizontal lines represent the quartiles (25th = 83 nm; 75th = 101 nm) and the median (93 nm) of two independent experiments, respectively. The median distance (n = 14) is indicated.

can also be bracketed by sites of different generations (Fig. 2B). We, therefore, based our classification on the diameter of the site considered with respect to that of its neighbors (Fig. 2C). We identified three classes of PG synthesis sites: the early-division class (E) harbors large diameters (>800 nm) and no visible constriction, the mid-division group (M) exhibits visible constriction (d_M) and neighboring sites that are even more constricted ($d < d_M$), and the late-division group (L) includes constricted sites (d_L) flanked by sites that are less constricted ($d > d_L$). Our analysis revealed that most of the PG synthesis sites fall into the late-division group in the Δ*divIVA* strain, with 30%, 17%, and 53% (n = 200) of the sites assigned to the early-, mid-, and late-division classes, respectively (Fig. 2D). To compare these proportions with that of the WT strain, the cell categories reported previously were converted into categories of labeled bands by adding two early-division sites for each late-division cell (Fig. S1B and S1D) since these were defined as displaying a constricted site surrounded by two new daughter sites (3). The division sites of the WT strain are, thus, distributed with proportions of early-, mid-, and late-division of 68%, 18%, and 14%, respectively. Since cells were labeled during steady-state growth, the proportion of each labeled sites reflects the relative duration of the corresponding stage

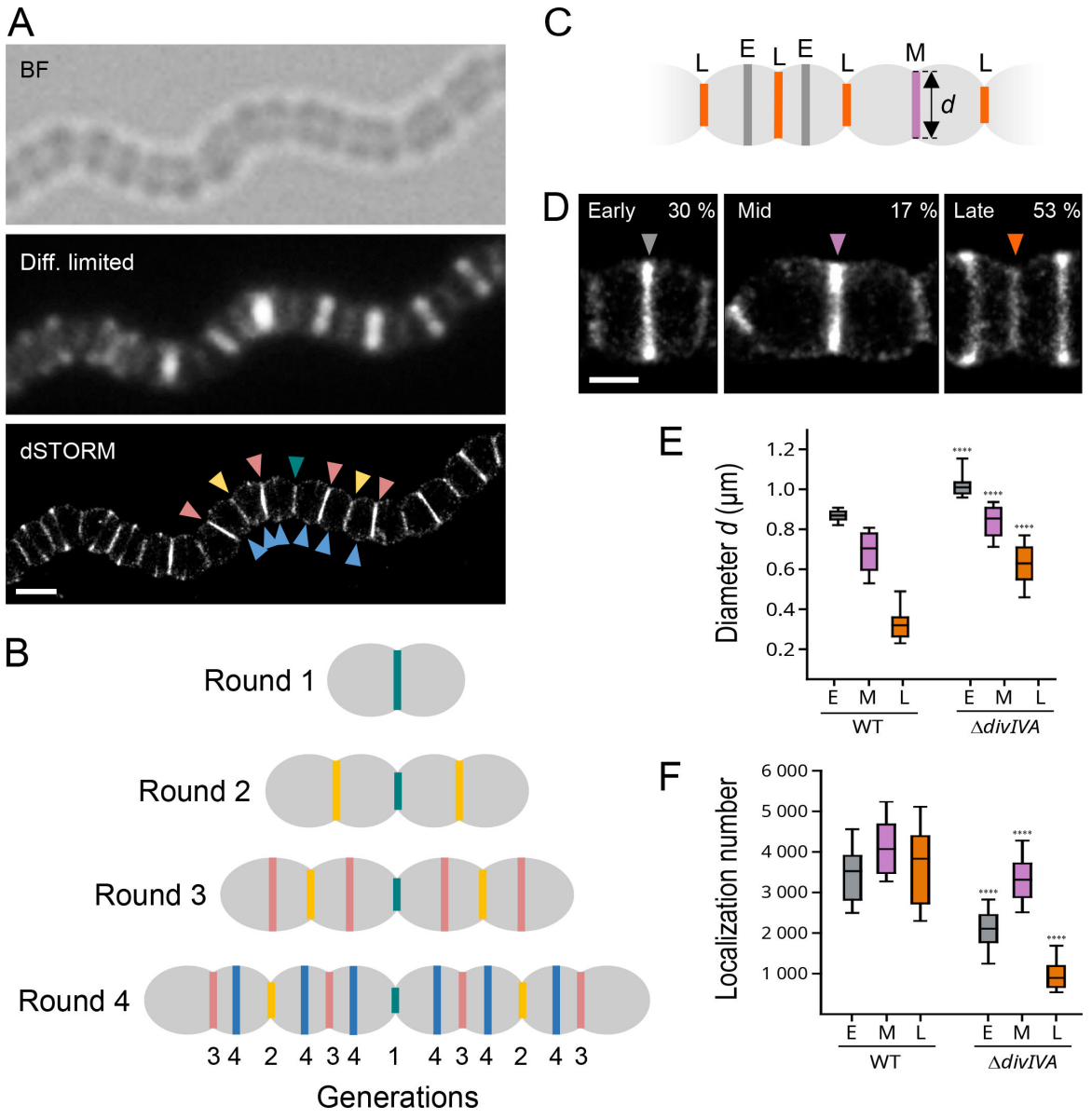

FIG 2 dSTORM analysis of PG synthesis in Δ*divIVA* cells. (A) *S. pneumoniae* Δ*divIVA* cells in the exponential growth phase were grown for 5 min in the presence of 2 mM aDA-DA, fixed, and incubated with 35 µM DIBO-AF647 for fluorescent labeling. Bright field (BF), fluorescence diffraction-limited (Diff. limited), and reconstructed dSTORM images are shown. The arrowheads point to division sites of different generations, with a color code identical to that of panel B. Scale bar, 500 nm. (B) Schematic illustration of the successive generations observed in Δ*divIVA* cell chains. First, second, third, and fourth generations are, respectively, indicated with teal, yellow, pink, and blue colors. (C) Schematic diagram of pulse-labeled Δ*divIVA* cells lying along their longitudinal axis. The dark gray, purple, and orange bands correspond, respectively, to early- (E), mid- (M), and late-division (L) pulse-labeling patterns, defined by their respective diameter (D). (D) Zoom on representative dSTORM images of Δ*divIVA* cells displaying early-, mid-, and late-division pulse-labeling patterns. Scale bar, 250 nm. (E) Distribution of the diameters *d* among early- (E), mid- (M), and late-division (L) pulse-labeling patterns in wild-type (WT) (*n* = 116) and Δ*divIVA* (*n* = 200) cell populations. (F) Distribution of the number of localizations among early- (E), mid- (M), and late-division (L) pulse-labeling patterns in wild-type (WT) (*n* = 116) and Δ*divIVA* (*n* = 200) cell populations. (E and F) Data are represented with box plots showing the interquartile range (10th and 90th percentile), the median value, and whiskers for minimum and maximum values. *P*-values from the *U* test of Mann-Whitney between WT and Δ*divIVA* data sets are indicated with quadruple asterisks when the observed difference is statistically significant (*P*-value < 0.0001).

of the cell cycle. In the absence of DivIVA, the late-division stage is, therefore, longer than the earlier stages. Consistent with this observation and with a defect in septum splitting, the median diameters of the labeling sites in the Δ*divIVA* strain are higher than in the WT strain (Fig. 2E).

Quantification of the number of localizations further shows that compared to the WT strain, less PG is synthesized in the absence of DivIVA (Fig. 2F). Whereas PG insertion remains robust along the whole cell cycle of WT cells, it dwindles to 27% of its maximum during late-division stages when *divIVA* is deleted. Also of note, the shortest labeled diameters measured in WT cells are at 150 nm, whereas the smallest diameter in the absence of DivIVA is about 280 nm (Fig. 2E). It is unclear whether cells fail to complete their cell division or if it continues at an extremely slow rate at which labeling is not detected.

The pneumococcal cell cycle consists of two elongation phases

When scanning Δ*divIVA* cell chains, symmetrical patterns, sometimes of up to seven bands, can be found (Fig. 3). This number indicates that following a round of division, the cell cycles of the descendants can remain synchronized for two more rounds of division (see Fig. 2B). Labeling bands arising from a fourth generation are much less frequent, implying that the rate of cell cycle progression between cells varies sufficiently to nullify synchronization beyond three or four generations. We distinguished four typical symmetrical patterns. In one pattern (Fig. 3A), four long weakly labeled bands (gray arrowheads, early stages) surround a short middle weakly labeled band (central orange arrowhead, late stage) and two strongly labeled bands of intermediate length (lateral orange arrowheads, late stage). In the second pattern (Fig. 3B), the central weakly labeled band (central orange arrowhead, late stage) is flanked by four strongly labeled bands (gray arrowheads, early stages), which sandwich two bands of smaller diameter (lateral orange arrowheads, late stages). The third pattern (Fig. 3C) is similar to the previous one, but the two small diameter bands show a weak labeling. A fourth pattern shows a series of weakly labeled bands (Fig. 3D).

To understand the dynamics of PG synthesis underlying the observed dSTORM patterns, we previously developed a dynamic geometrical model of cell wall expansion. This model was parametrized using measurements taken on experimental data and could successfully recapitulate the labeling patterns of the WT strain (Fig. S1B) (3). Interestingly, to reproduce the patterns obtained with the Δ*divIVA* strain, this model had to be refined. Whereas modeling data from WT strains required an acceleration of the elongation rate to account for the thickening of the labeling bands along the cell cycle (3), the statistics of the band diameters and number of localizations measured for the Δ*divIVA* mutant (Fig. 2E and F) suggested a deceleration of the cell elongation. Different functions were trialed to model a deceleration of the elongation rate, but the morphology of the Δ*divIVA* strain and the labeling patterns could best and most simply be mimicked with two successive phases of constant elongation rates. Two additional parameters were, thus, added to the model to define when the second phase starts, and how reduced is its rate compared to the first phase. The absence of small labeled rings was modeled by a complete stop of the cell cycle at a fraction of the full cell length. The other parameters of the model remain. Regarding the cells, they are the length/diameter ratio, the time of completion of the septum closure, and the time of the start of the next generation. Regarding the labeling patterns, the parameters are the start and the length of the pulse. In contrast to the WT strain for which the values of the parameters were obtained by fitting of the model functions to experimental measurements (3), the number of measurable, well-defined symmetrical patterns of the different types was not sufficient to perform meaningful fitting. Instead, the values of the parameters were manually adjusted to best represent the Δ*divIVA* observations. The modeled labeling patterns and cell wall representations are shown alongside dSTORM images in Fig. 3. The chosen values are given in Table 1. Graphs of the modeled evolution of the cell length and outer and inner diameter of the septum with the chosen parameters are given in Fig. S3. The first pattern (Fig. 3A) is produced when the labeling takes place when the second generation (yellow arrowheads) is producing most of its septum, whereas the septum of the first generation (teal arrowhead) has already closed and the third-generation division has just started (pink arrowheads) (see Fig. S3 for the position of the green labeling

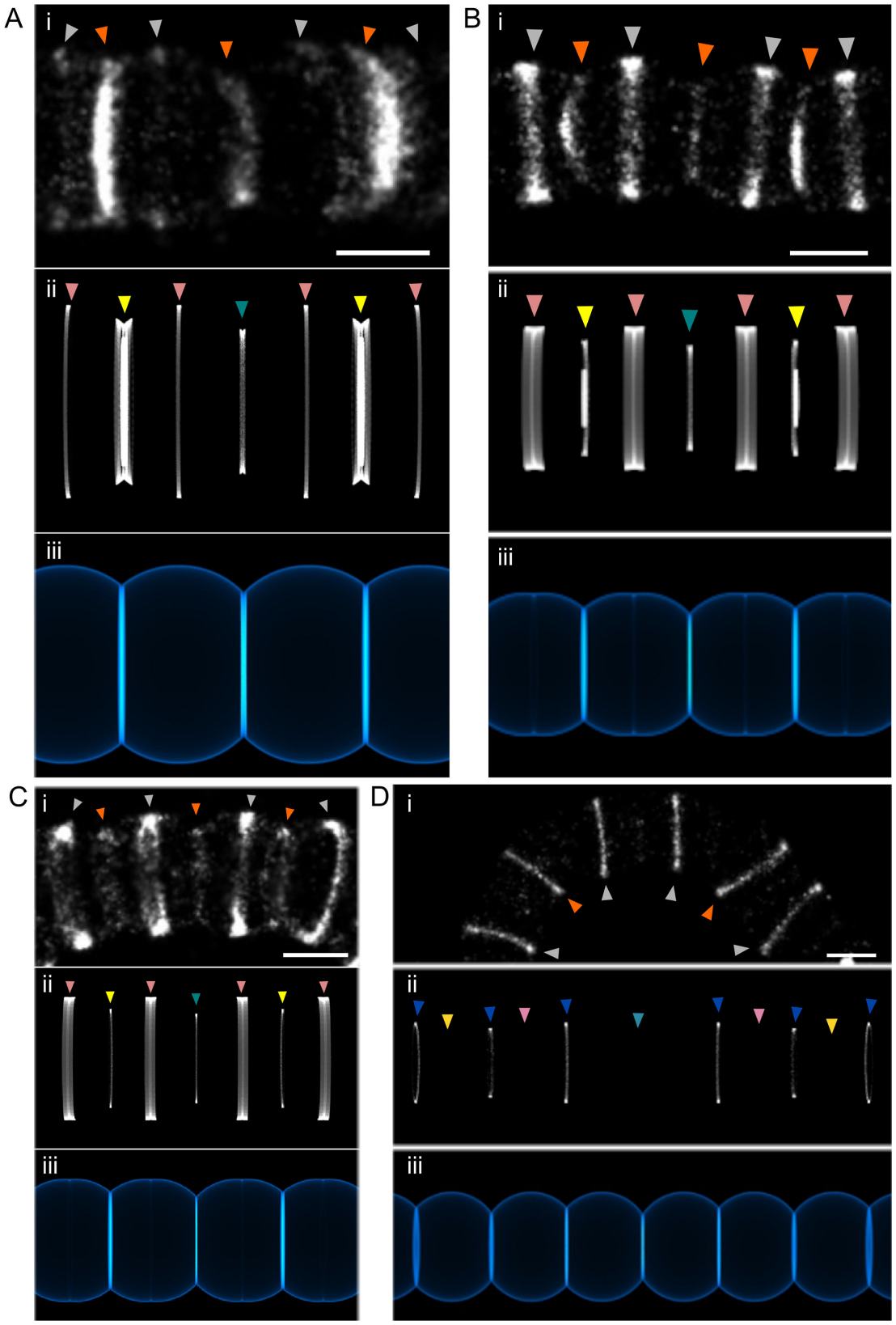

FIG 3 Symmetrical banding patterns are reproduced by a dynamic geometrical model of cell wall growth. *S. pneumoniae* Δ*divIVA* cells in the exponential growth phase were grown for 15 min (A and B) or 5 min (C and D) in the presence of 2 mM aDA-DA, fixed, and incubated with 35 µM DIBO-AF647 for fluorescent labeling. Reconstructed dSTORM (i), simulated labeling patterns (ii), and corresponding simulated cell wall (iii) images are shown. Arrowheads point to equivalent

(Continued on next page)

Fig 3 (Continued)

labeling bands generated either experimentally (i) or by *in silico* modeling (ii). In panel (i), arrowheads colored in gray and orange indicate, respectively, early- and late-division sites, as in Fig. 2C. In panel (ii), arrowheads colored in teal, yellow, pink, and blue colors indicate, respectively, first, second, third, and fourth generations, as in Fig. 2B. Scale bars, 500 nm. The same model parameters given in Table 1 were used for all the patterns, while the timing and duration of the labeling pulse were changed to generate each pattern (see Fig. S3).

pulse). In the second pattern (Fig. 3B), the pulse starts slightly later, while septum synthesis of the second generation is already well advanced (Fig. S3, orange labeling pulse). To generate the third pattern (Fig. 3C), a short pulse occurs as the third-division cycle is in the first (fast) phase, whereas the second- and first-generation cycles are in the second slower phase and after septal closure (Fig. S3, cyan labeling pulse). The weak labeling is the result of slow peripheral PG insertion. The fourth pattern (Fig. 3D) appears when the labeling pulse occurs while three successive divisions have closed their septum and ceased to incorporate PG material but a fourth division (blue arrowheads) has just started (Fig. S3, yellow labeling pulse). The experimental data acquired on the Δ*divIVA* strain are, thus, consistent with a biphasic model of the pneumococcal cell cycle in which the elongation rate is reduced during the second phase.

Septal synthesis is maintained, but septum splitting and peripheral synthesis are impaired in the absence of DivIVA

To further analyze the dynamics of PG synthesis in the Δ*divIVA* strain, we analyzed tilted cells in which the radial architecture of the labeled regions can be observed (Fig. 4A). To account for the difference in cell diameter between the WT and Δ*divIVA* strains, we normalized the width of the septal plate (measured as the distance *r*, Fig. 4B) to the mean value of early-stage labeling diameters ($d(E)_{WT}$ = 850 nm; $d(E)_{\Delta divIVA}$ = 980 nm), as those have not yet initiated constriction. At mid- and late-division stages, the *r*/*d*(*E*) ratio is greater than in the WT strain (Fig. 4C), consistent with active septal PG synthesis and defective septum splitting in Δ*divIVA* cells. In this orientation, WT cells at mid- and late-division stages show inner and outer labeling rings, respectively, corresponding to septal and peripheral PG synthesis (Fig. 4A, patterns *d* to *f*) (3). Cells harboring these concentric patterns represent 4% (*n* = 148) of the whole WT cell population. In Δ*divIVA* cells, similar concentric patterns are observed in a larger proportion of the cell population (15%, *n* = 148) (Fig. 4A, patterns *c* to *f*), which is consistent with impaired septum splitting. Indeed, since septal PG is synthesized at the leading edge of the growing septum and peripheral PG is synthesized at its periphery, deficient cleavage of the septum favors the separation of the two sites of synthesis. The experimental labeling patterns were correctly reproduced when septal synthesis was maintained until septum closure, and the rate of septum splitting and concomitant peripheral PG insertion was severely reduced in a second phase of the cell cycle (Fig. 4A).

The dynamics of septum splitting and peripheral synthesis, or in other words cell elongation, were previously documented for WT strains using pulse-chase labeling

TABLE 1 Parameters of the geometrical model used to simulate the cell wall growth

Strain		WT[a]	*ΔdivIVA*
Diameter	*D* (µm)	0.85	0.98
Length	*L* (µm)	1.05	0.91
Elliptic ratio	*E* = *L*/*D*	1.24	0.93
Start of next generation as a fraction of the generation time	*N*	0.9	0.68
Acceleration factor	*A*	0.9	0
Septum closure as a fraction of generation time	*C*	0.84	0.68
Time of slowing elongation as a fraction of generation time	T_S	n/a	0.58
"Brake" factor	*B*	n/a	0.13
Fraction of complete length at which all processes stop	*S*	n/a	0.8

[a]Reported from reference (3).

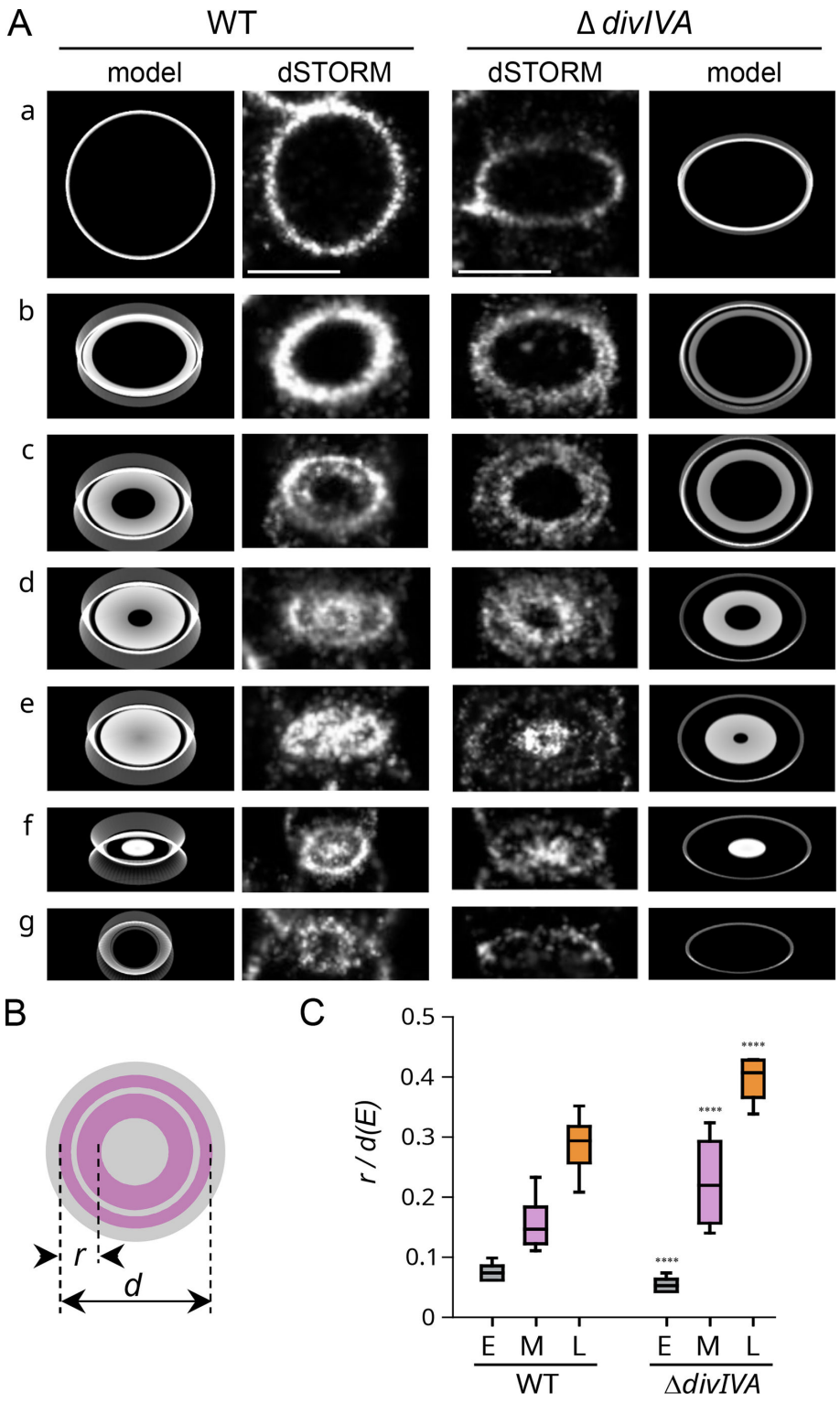

FIG 4 PG synthesis observed in tilted cells. (A) Typical dSTORM localization patterns of pulse-labeled PG in cells oriented vertically or at an angle in an agarose pad. Early- to late-division stages are shown from top to bottom panels (a–g). Exponentially growing wild-type (WT) and Δ*divIVA* cells were incubated for 5 min with aDA-DA, fixed and labeled with DIBO-AF647 before being trapped below an agarose pad. Scale bars, 500 nm. (B) Schematic diagram representing a mid-division cell oriented perpendicular to its longitudinal axis. This orientation allows observing the septal (inner ring) and peripheral (outer ring) PG synthesis sites and measuring the radial width (*r*) of the labeled region. (C) Distribution of the radial

(Continued on next page)

Fig 4 (Continued)

width of labeling *r*, normalized to the median largest diameter *d(E)* in early- (E), mid- (M), and late-division (L) pulse-labeling patterns in WT (*n* = 170) and Δ*divIVA* (*n* = 149) cell populations. Data are represented with box plots showing the interquartile range (10th and 90th percentile), the median value, and whiskers for minimum and maximum values. The quadruple asterisks represent a statistically significant difference between WT and Δ*divIVA* data sets (*U* test of Mann-Whitney, *P*-value < 0.0001).

experiments (3). Pulse-labeled PG is remodeled during the chase period, resulting in pulse-chase localization patterns that are wider than pulse patterns. In our model of pneumococcal PG synthesis, the septal PG is rapidly cleaved during early division so that it is repositioned as hemispheric wall almost immediately after synthesis (Fig. S1A) (3). In a WT strain, when this stage (E) is observed in a pulse-chase experiment, the pulse-labeled PG splits into two bands during the chase due to the synthesis of unlabeled PG at mid-cell (Fig. 5A, gray arrowhead). At mid- (M) and late- (L) division stages, septum cleavage lags behind septal PG synthesis, resulting in septum formation. In a pulse-chase experiment, a labeled septum is formed during the pulse and is cleaved during the chase. The cell wall that is repositioned laterally during the chase, thus, contains a mixture of labeled septally synthesized PG and unlabeled peripheral PG (3). Such remodeling appears as "butterfly-like" patterns (Fig. 5A, violet and orange arrowheads). Throughout the cell cycle, the rate of septal cleavage and peripheral PG insertion can be assessed by measuring the "width of the chase" (W_{CHASE}), which is the distance separating the external borders of the labeled patterns in pulse-chased cells (Fig. 5B).

During early division, the median width of the chased region in Δ*divIVA* cells (W_{CHASE}(E) = 270 nm, *n* = 119) is rather similar to that of the WT strain (W_{CHASE}(E) = 260 nm, *n* = 123) (Fig. 5C). By contrast, W_{CHASE} is reduced in the absence of DivIVA at mid- (W_{CHASE}(M) = 280 nm, *n* = 57) and in particular at late division (W_{CHASE}(L) = 80 nm, *n* = 162) when compared to the WT strain (W_{CHASE}(M) = 415 nm, *n* = 122; W_{CHASE}(L) = 430 nm, *n* = 119). These measurements confirm that elongation slows down dramatically during the cell cycle in the absence of DivIVA, whereas it accelerates in the WT strain. The geometrical model correctly reproduces the observed chased patterns (Fig. 5D). Only sites that were labeled early during the first phase of rapid PG synthesis show significant parting of split labeled bands. Sites that were labeled late during the first (rapid) phase or during the second (slow) phase show little splitting of the bands.

In addition to the double-band patterns described above, 10% of the Δ*divIVA* early-division sites (*n* = 301) showed asymmetric separation of the labeled region, resulting in "Y-like" localization patterns (Fig. 5E). This proportion is probably underestimated since it only includes "Y-like" patterns correctly oriented in the *XY* plane and does not consider similar patterns oriented in the *Z* axis. Asymmetric pulse-chase labeling patterns are never observed in early-division WT cells, in which pulse-labeled regions are always chased as parallel bands (Fig. 5A). In the absence of DivIVA, the presence of Y-like labelings indicate that septal splitting and associated peripheral PG synthesis are non-uniformly distributed around the division site.

The contribution of the elongasome and aPBPs to cell elongation is modified in the absence of DivIVA

S. pneumoniae cell elongation is known to rely on peripheral PG synthesis by the elongasome, which is formed by the RodA/bPBP2b pair (19, 32, 46). On the other hand, given that peripheral PG is inserted into cleaved septal regions and that septal PG is modified by aPBPs (3, 21), it is possible that aPBPs influence peripheral PG insertion and, thus, cell elongation. Since the later process is impaired in Δ*divIVA* cells, we sought to investigate the interplay between DivIVA and the elongasome or aPBPs using pulse-chase experiments (Fig. 6A and C; Fig. S4A). Consistent with a previous study by Tsui et al., the deletion of *pbp2b* in a WT background required the combined inactivation of *mltG*, which was obtained by mutating the catalytic tyrosine (Y488D mutation) (28). Measurement of W_{CHASE} was used to estimate the cell elongation (Fig. 6B and D; Fig.

S4B). Compared to WT cells, W_{CHASE} is reduced by a factor of 1.4, 1.5, and 1.6 at early-, mid-, and late-division stages in Δ*pbp2b mltG*$_{Y488D}$ cells (Fig. 6B). In a WT background,

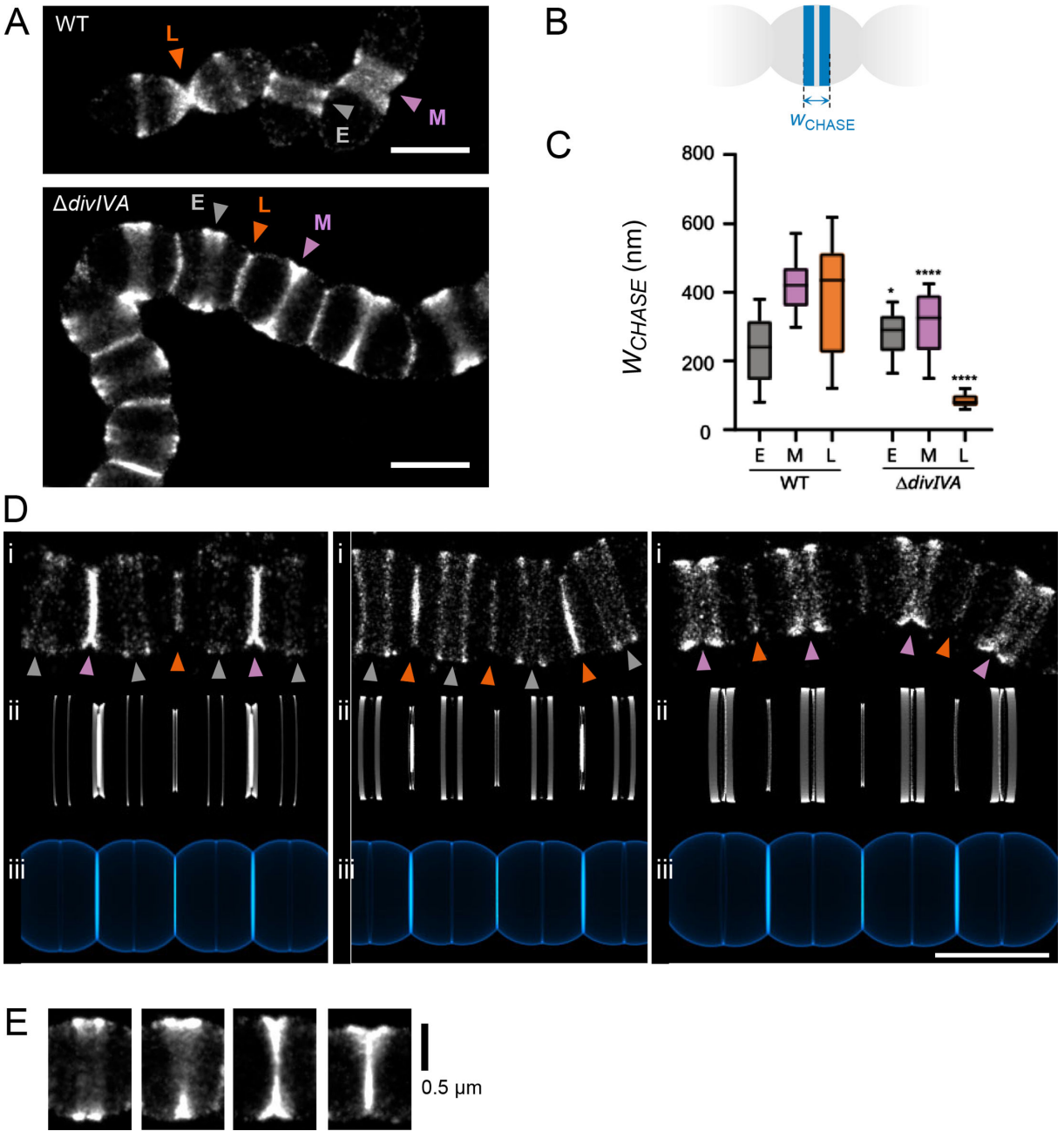

FIG 5 Pulse-chase labeling patterns of *ΔdivIVA* cells. (A) Representative dSTORM images of pulse-chase localization patterns in wild-type (WT) and *ΔdivIVA* cells. Exponentially growing cells were incubated for 5 min with aDA-DA (pulse), grown for 15 min in the absence of the probe (chase), fixed, and labeled with DIBO-AF647 before dSTORM data collection. The gray, violet, and orange arrowheads point to early-, mid-, and late-division sites, respectively. Scale bars, 1 µm. (B) Schematic representation of a pulse-chase labeled cell harboring two bands at an early-division site. The distance (W_{CHASE}) separating the longitudinal outer limits of the labeling pattern is shown. (C) Distributions of the W_{CHASE} of the labeling patterns in early- (E), mid- (M), and late-division (L) sites [WT, *n*(E) = 89, *n*(M) = 68, and *n*(L) = 12; *ΔdivIVA*, *n*(E) = 43, *n*(M) = 34 cells, and *n*(L) = 101]. Data are represented with box plots showing the interquartile range (10th and 90th percentile), the median value, and whiskers for minimum and maximum values. *P*-values from the *U* test of Mann-Whitney between different data sets are indicated with single or quadruple asterisks when the observed differences are statistically significant with *P*-values < 0.01 or <0.0001, respectively. (D) Typical symmetrical dSTORM localization patterns of pulse-chase labeled PG in *ΔdivIVA* cells. Earlier to later division stages are shown from left to right Panels. Panels (i), (ii), and (iii) are dSTORM images, simulations of the labeling patterns, and corresponding cell wall, respectively. Scale bar, 1 µm. (E) dSTORM images of asymmetrical pulse-chase labeling patterns found with *ΔdivIVA* cells.

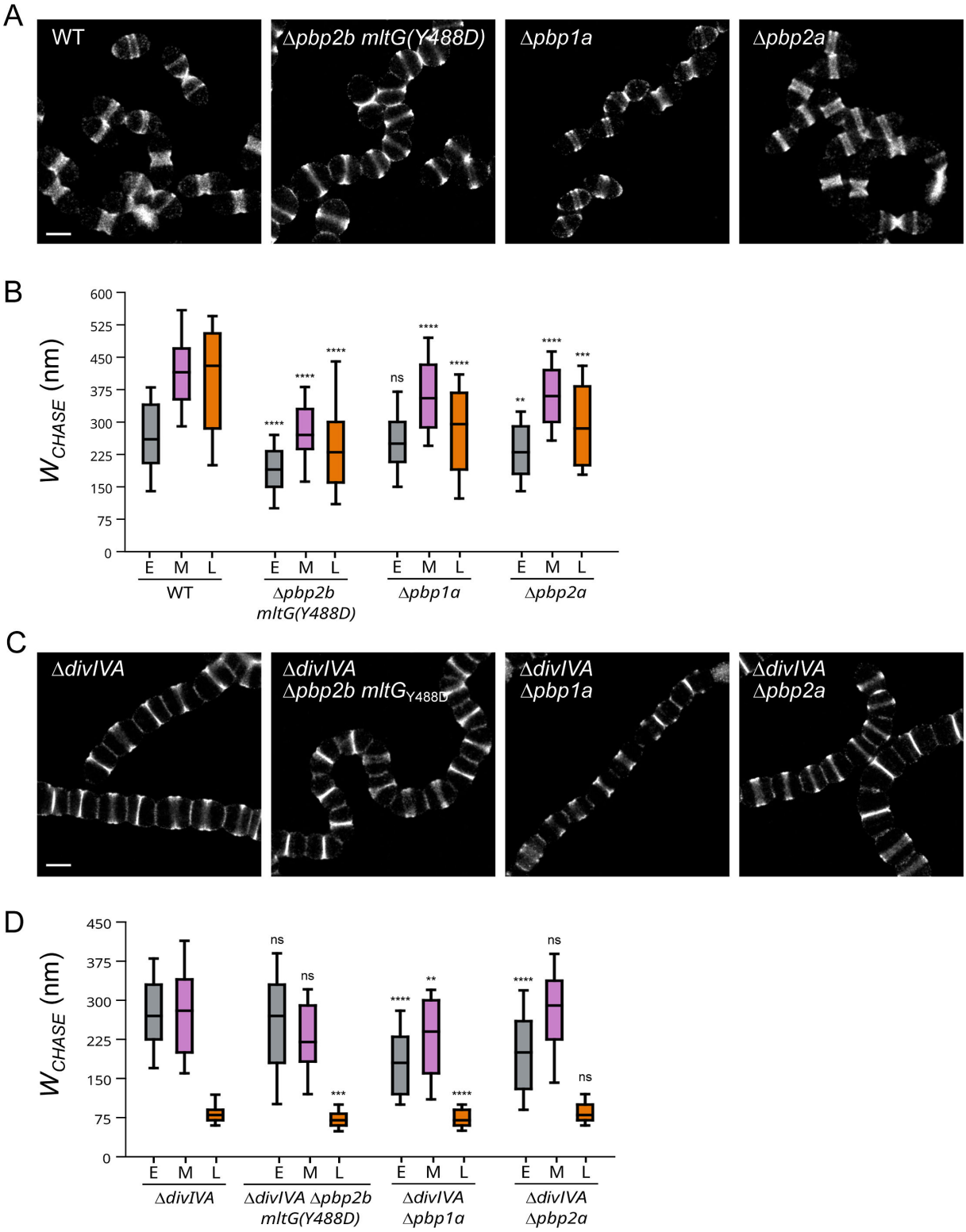

FIG 6 Effect of *pbp* gene deletion on *ΔdivIVA* pulse-chase labeling patterns. (A) Fields of wild-type (WT), Δ*pbp2b mltG(Y488D)*, Δ*pbp1a,* and Δ*pbp2a* cells treated with the pulse-chase labeling protocol and observed by dSTORM. Scale bar, 1 µm. (B) Distributions of W_{CHASE} of the pulse-chase labeling patterns observed in panel A (WT, *n*(E) = 132, *n*(M) = 123, and *n*(L) = 46; Δ*pbp2b mltG*(Y488D), *n*(E) = 148, *n*(M) = 84, and *n*(L) = 65 cells; Δ*pbp1a*, *n*(E) = 140, *n*(M) = 116, and *n*(L) = 42 cells; Δ*pbp2a*, *n*(E) = 109, *n*(M) = 108, and *n*(L) = 40 cells). (C). Fields of Δ*divIVA* mutant strain cells treated with the pulse-chase labeling protocol and observed by dSTORM. Scale bar, 1 µm. (D) Distributions of W_{CHASE} of the pulse-chase labeling patterns observed in panel C [Δ*divIVA*, *n*(E) = 120, *n*(M) = 57, and *n*(L) = 172

(Continued on next page)

Fig 6 (Continued)

cells; Δ*divIVA* Δ*pbp2b mltG(Y488D)*, *n*(E) = 132, *n*(M) = 50, and *n*(L) = 120 cells; Δ*divIVA* Δ*pbp1a*, *n*(E) = 121, *n*(M) = 71, and *n*(L) =109 cells; Δ*divIVA* Δ*pbp2a*, *n*(E) = 112, *n*(M) = 42, and *n*(L) =146 cells]. (B and D) Data are represented with box plots showing the interquartile range (10th and 90th percentile), the median value, and whiskers for minimum and maximum values. *P*-values from the *U* test of Mann-Whitney between different data sets are indicated with double asterisks when *P*-values < 0.01, triple asterisks when *P*-value < 0.001, quadruple asterisks when *P*-values < 0.0001, or with "ns" when no significant difference is observed (*P*-value > 0.05).

bPBP2b-based peripheral PG synthesis is, therefore, a major contributor to all elongation phases. Interestingly, cell elongation is also diminished in mid- to late-division stages in the absence of aPBP1a or aPBP2a.

bPBP2b was previously shown to remain localized and essential in the absence of DivIVA (36). As in a WT strain, we, thus, inactivated MltG to suppress the requirement for bPBP2b. However, in the Δ*divIVA* background, bPBP2b inactivation had a milder effect on cell elongation. Indeed, compared to Δ*divIVA* cells, W_{CHASE} is either not reduced during early- and mid-division, or reduced by a factor of 1.2 at the late-division stage in Δ*divIVA* Δ*pbp2b mltG*$_{Y488D}$ cells (Fig. 6D). In the absence of DivIVA, the elongasome contribution to the cell elongation is, thus, diminished all along the cell cycle.

Inspection of aPBP1a localization using an ectopic GFP fusion protein showed that it remains positioned at PG synthesis sites in Δ*divIVA* cells (Fig. S5A). However, the comparison of the width of the chase between Δ*divIVA* and Δ*divIVA* Δ*pbp1a* cells shows a reduction in cell elongation at all stages of the cell cycle, especially in early- and late-division stages, upon *pbp1a* deletion (Fig. 6D). This is slightly different from the WT strain, in which the absence of aPBP1a has no effect on W_{CHASE} during early-division (Fig. 6B). In a WT genetic background, the contribution of aPBP1a to early-elongation is probably masked by the strong contribution of the elongasome. The contribution of aPBP1a to early-division is, therefore, revealed by the absence of DivIVA, as the role of bPBP2b is minimal in this genetic background. In Δ*divIVA* cells, aPBP1a appears important for cell elongation all along the cell cycle.

The effect of *divIVA* deletion on aPBP2a localization could not be investigated because an ectopic GFP-aPBP2a fusion protein is likely not functional as it does not localize exclusively at mid-cell in WT cells and, therefore, a fortiori in Δ*divIVA* cells (Fig. S5B). The pulse-chase experiments, however, revealed differences in the contribution of aPBP2a to cell elongation in the presence or absence of DivIVA. In WT cells, aPBP2a mainly contributes to mid- and late-division stages (Fig. 6B). By contrast, in Δ*divIVA* Δ*pbp2a* cells, W_{CHASE} does not decrease at these stages compared to Δ*divIVA* cells, indicating a decreased participation of aPBP2a to cell elongation in the absence of DivIVA (Fig. 6D). On the other hand, when compared to Δ*divIVA* cells, W_{CHASE} is reduced by a factor of 1.4 during early-division in Δ*divIVA* Δ*pbp2a* cells. Here again, the role of aPBP2a during early cell elongation is, therefore, revealed in the absence of DivIVA.

In conclusion, the absence of DivIVA affects not only peripheral PG synthesis by the elongasome but also the contribution of aPBP1a and aPBP2a to cell elongation.

DISCUSSION

DivIVA is anchored in the plasma membrane by an N-terminal motif composed of a hydrophobic residue flanked by positively charged amino acids (47, 48). The central part of DivIVA forms coiled coils of varying length in different Gram-positive species. It assembles as a tetramer formed by the antiparallel association of two parallel coiled-coil dimers. Depending on the organism, there is an additional non-conserved C-terminal tail. Tetramers of DivIVA from *Bacillus subtilis* were found to assemble *in vitro* into large lattice-like structures (48). Most importantly, DivIVA binds preferentially to negatively curved membrane regions (40, 49), which accounts for its concentration at the cell poles and as two rings bordering the invaginating membrane, as previously reported for *B. subtilis* (39, 44, 45), and established in this work for *S. pneumoniae*.

As a scaffold protein with an affinity for negatively curved membranes (40, 49), DivIVA may have been used and reused by the mechanisms of evolution as a platform for processes that must occur at such places in bacteria. For example, DivIVA directs apical growth in corynebacteria and mycobacteria (50, 51), it participates indirectly in positioning of the division site in *B. subtilis* by interacting with the Min system (44, 52), and it is involved in chromosome partitioning by positioning the ParB protein at the cell poles in *Corynebacterium glutamicum* (53). In ovococci such as *S. pneumoniae*, the absence of DivIVA causes major morphological defects, as the Δ*divIVA* strain grows as chains of lentil-shaped cells, compressed in the direction of the long axis [this work and (19, 36)]. DivIVA is, thus, required for proper ovoid shape, but how does it fulfill its morphogenetic function?

Here, we have shown that in *S. pneumoniae*, DivIVA is more concentrated at the division site than at the cell poles, suggesting that it plays a major function at the sites of active PG synthesis. The current model proposes that the ovoid shape of *S. pneumoniae* results from a finely balanced and interconnected synthesis of septal and peripheral PG, respectively, required for cell division and elongation. The latter is thought to result primarily from the action of the RodA/bPBP2b glycosyltransferase/transpeptidase couple associated with the hydrolase MltG/MpgA. Indeed, the absence of a functional elongasome (RodA/bPBP2b/MltG) engenders chains of shorter cells [this work and (19, 54)], and our dSTORM data show that elongation is actually impaired at all stages of the cell cycle. Cells without DivIVA display a similar morphology, but we show, in this case, that elongation is only impaired at the mid and late stages of the cell cycle. Surprisingly, in the same cells, the elongasome appears to be inactive in the early and mid stages. Early elongation in Δ*divIVA* cells must, therefore, rely on another machinery than the elongasome. Observations made in aPBP mutants may shed some light on this. Indeed, in the absence of DivIVA, our data reveal a contribution of aPBP1a and aPBP2a to early elongation that is not detected in an otherwise WT background. Therefore, DivIVA seems to affect in some way the function of the elongasome and aPBPs, whose contribution to cell elongation seems to compensate each other during the early stage of the cell cycle.

Regardless of the enzymatic machineries involved, a major observation allowed by our dSTORM data is the existence of two cell growth phases during the pneumococcal cell cycle, as the absence of DivIVA does not affect early elongation (first phase) but dramatically impairs mid and late growth stages (second phase). More precisely, septation proceeds normally during the second phase but splitting of the septum and concomitant peripheral synthesis are drastically slowed down, leading to chains of shorter cells. From different attempts at simulating the labeling patterns with a geometrical model of the cell growth, it appears that the deceleration of septum splitting and peripheral synthesis must be abrupt rather than gradual. Later, it is possible that the elongation process ceases completely as no labeling of division sites of small diameter could be detected. Since long Δ*divIVA* cell chains still have extremities, the division of some rare cells may proceed to completion through septal splitting possibly decoupled from peripheral synthesis. Alternatively, long chains may be broken by the occasional lysis of some cells.

Also very interestingly, the resolution attained by dSTORM in pulse-chase labeling experiments has revealed Y-shaped labeling patterns in Δ*divIVA* cells, while pulse-labeled regions are always chased as parallel labeling rings in WT cells. These observations suggest that during the chase time, the elongation due to septal splitting and peripheral synthesis sometimes progresses at different speeds along the perimeter of the septum in the Δ*divIVA* strain, whereas the rate of elongation is identical around the septal circumference in WT cells.

Our detailed dSTORM localization of PG assembly in a *divIVA* deletion strain, thus, shows that DivIVA is necessary (i) to maintain elongation passed a threshold time point during the cell cycle and (ii) to coordinate the related processes around the mid-cell perimeter. How can DivIVA achieve such temporal and spatial regulation? Interestingly, the bi-phasic elongation process evidenced in this work is reminiscent of the bi-phasic

dynamic behavior of DivIVA, which was shown to move in a directed manner around early-division sites and more diffusively around mid- and late-division sites (17). A hypothesis that would unify all the observations reported to date would, thus, be to consider that DivIVA is a physical sensor of membrane curvature, which would guide its localization in regions where septum splitting and peripheral synthesis need to be stimulated.

Although speculative, let us first consider how should evolve the force that favors septum splitting (Fig. 7A). The surface tension resulting from the turgor pressure ΔP is $\gamma = \Delta PR/4$, where R is the radius of curvature. At the junction of the septal and peripheral surfaces, for every segment s of the circumference of the septum, this surface tension generates a force, tangential to the peripheral surface away from the septum with a value $|\overrightarrow{F}_s| = \gamma s$. This force can be decomposed in a component parallel to the septal plane $|\overrightarrow{F}_{||}| = \cos\theta|\overrightarrow{F}_s|$, and a component perpendicular to the septal plane $|\overrightarrow{F}_{\perp}| = \sin\theta|\overrightarrow{F}_s|$, where θ is the angle between the new peripheral wall and the septal wall. This angle is $\pi/2$ at the start and increases toward π at the end of the division. Therefore, the component perpendicular to the septal plane $\overrightarrow{F}_{\perp}$, which should help tearing apart the septum, progressively vanishes as the division progresses. A good analogy of this phenomenon is the removal of an adhesive tape from a surface: it is easier if you pull perpendicularly to the surface than if you pull at a shallow angle. Thus, the turgor pressure and the cell geometry provide a force $\overrightarrow{F}_{\perp}$ that can help septum splitting. The stretched septal PG at the periphery could be a better substrate for the cleaving enzyme.

The fact that, in the absence of DivIVA, septum splitting and associated peripheral PG synthesis proceed normally during early division and then slows dramatically, suggests that a different or autonomous driving force exists at the beginning but is not present at the end of the process. The mechanical force $\overrightarrow{F}_{\perp}$ described above could fulfill this role since it diminishes necessarily during cell separation (Fig. 7A). This waning force could reach a threshold where it is not sufficient and DivIVA would kick-in to stimulate further septum splitting. DivIVA, by virtue of its affinity for negatively curved membranes would be pre-localized exactly where required. In this scheme, DivIVA may be considered an activator of septum splitting and the associated peripheral PG synthesis. How DivIVA achieves such activation remains mysterious. One common hypothesis is to propose that DivIVA acts as a platform protein that interacts directly or indirectly with proteins of the cell wall metabolism to concentrate them and/or activate them at specific locations. In this model, the accumulation of DivIVA at PG synthesis sites would be correlated with the acceleration of cell elongation reported previously in *S. pneumoniae* and *C. glutamicum* (3, 55). Based on the defective peripheral synthesis observed in pneumococcal Δ*divIVA* cells, elongasome proteins appear as putative partners of DivIVA. In agreement with this idea, DivIVA was shown to localize RodA in *C. glutamicum* and MltG/MpgA in *Streptococcus suis* through direct physical interactions (38, 56). In these organisms, MltG/MpgA and RodA might, thus, use DivIVA as a localization platform. In *S. pneumoniae,* however, bPBP2b and RodA remain localized at division sites in the absence of DivIVA (36) although we cannot exclude that DivIVA induces local variations in bPBP2b and/or RodA concentrations that were not detected. If the pneumococcal DivIVA recruits neither RodA nor bPBP2b, an alternative hypothesis would be that DivIVA might indirectly activate peripheral synthesis, again through a physical mechanism based on its negative-curve affinity (Fig. 7B). Although the following hypothesis is again speculative, it is nevertheless consistent with the bi-phasic phenotype of Δ*divIVA* cells. Let us assume two additional features for the DivIVA lattice: a resting conformational angle ϕ_{rest} in the longitudinal plane comprised somewhere between $\pi/2$ and π, and anchoring points to the cell wall at both extremities (through some relay proteins). At the beginning of the division, the angle formed by the DivIVA lattice (ϕ) would be greater than that of the membrane at the periphery of the septum ($\phi = \phi_{rest} > \theta$). Since θ increases as the septum is cleaved, at some point, the DivIVA-lattice resting angle becomes smaller than

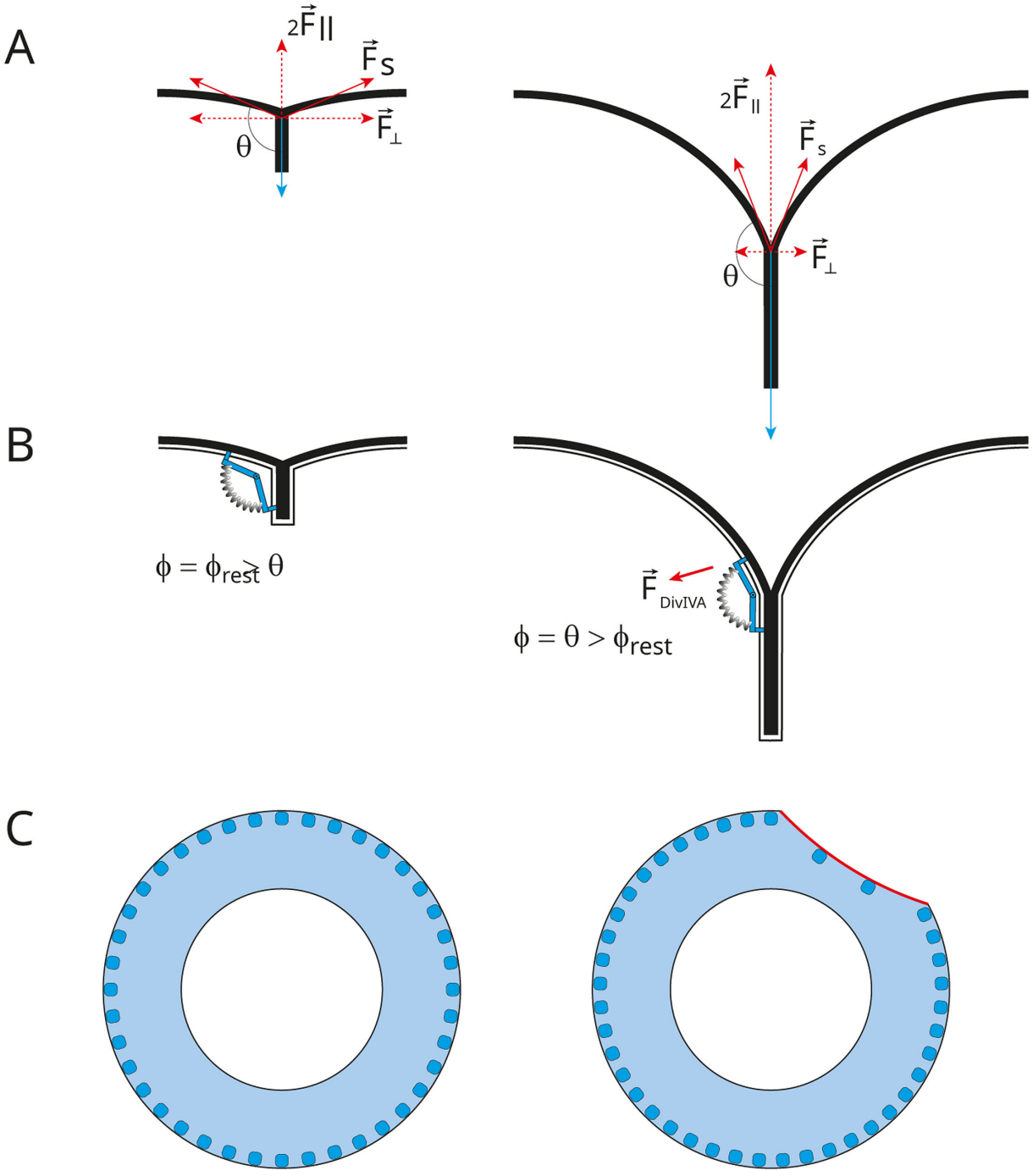

FIG 7 Model for the role of DivIVA in maintaining homogenous septum remodeling and peripheral PG synthesis in space and time. (A) Schematic representation of the division site, with θ being the angle between the septal and peripheral walls and $|\vec{F}_s|$ the tangential force exerted by the turgor pressure at the site of septum cleavage. Taking the septal plane as a reference, $|\vec{F}_s|$ can be decomposed in a parallel ($|\vec{F}_{||}| = \cos\theta|\vec{F}_s|$) and a perpendicular ($|\vec{F}_{\perp}| = \sin\theta|\vec{F}_s|$) component. $\vec{F}_{\perp}$, which contributes to septal PG cleavage, and decreases as the septum splits to generate new hemispheres. (B) In virtue of its polymeric nature and affinity for negatively curved membranes, the DivIVA lattice might display a conformation of minimal energy defined by a resting angle (ϕ_{rest}). Once ϕ_{rest} becomes smaller than θ, stretching of the DivIVA matrix would generate a force that compensates the vanishing of the $\vec{F}_{\perp}$ force, or activates the septum remodeling machinery. (C) Schematic representation of how negative curvature affinity of DivIVA (blue dots) could ensure uniform progression of splitting and peripheral synthesis around the septum (blue ring). If splitting/peripheral synthesis occurs along one section of the septum (red), the membrane curvature along this section decreases, leading to a reduced concentration of DivIVA. The reduced amount of DivIVA would slow down the splitting/synthesis in this region in comparison to the rest of the periphery, thus restoring a uniform progression around the division site.

that of the membrane ($\phi_{rest} < \theta$) and the DivIVA lattice would be stretched ($\phi = \theta$). In this new configuration, DivIVA experiences a tension that may be translated into an activation signal to interacting PG synthases/hydrolases, or it could transfer tension to the periphery of the septal PG itself, taking over the function of the diminishing splitting force $\overrightarrow{F}_{\perp}$. Note that the two hypothetical modes of action are not mutually exclusive.

If the affinity of DivIVA for the membrane increases with the curvature, and if septum splitting and peripheral synthesis are positively regulated by the presence of DivIVA, these two conditions would ensure an orderly symmetrical proceeding of the division around the cell circumference. If division were to occur faster in one region of the circumference (Fig. 7C right), the peripheral membrane curvature in that region would become smaller than in the rest of the cell circumference; the concentration of DivIVA would then decrease in this region of faster division and increase elsewhere, where it would stimulate the process. The sliding and modification of the local concentration of DivIVA along the septal circumference according to membrane curvature would, thus, automatically adjust the amount of cell wall metabolism required to ensure the even progression of the division. In Δ*divIVA* cells, heterogeneous septum splitting and/or peripheral synthesis would not be corrected by DivIVA, resulting in circularly asymmetrical PG labeling profiles, observed as Y-shaped labeling patterns in our dSTORM images.

The biphasic dynamic behavior of DivIVA evidenced by Perez et al. can also be explained by its affinity for negatively curved membranes (17, 40, 49). When the septum is not yet formed, if FtsZ drives membrane invagination at the division site, places of maximal negative membrane curvature necessarily follow the localization of the Z-ring around the cell perimeter. The affinity of DivIVA for negative membrane curvature would result in DivIVA moving directionally around the mid-cell circumference, seemingly "following" FtsZ treadmilling during early division. Past the very early stage, a large negative curvature is established at the periphery of the septal plate, whereas FtsZ remains localized at the leading edge of the closing septum. Consequently, the positioning of DivIVA would not depend on FtsZ treadmilling after the initial moments of the cell division process. At these later stages, the localization of DivIVA molecules around the septal periphery would depend on the modulation of the negative curvatures resulting from septum splitting, as proposed above.

Although the mode of action of DivIVA remains to be elucidated, our work improves our understanding of the cell cycle in *S. pneumoniae* and highlights a regulatory function for DivIVA. It sets the ground for further investigation, which should include cellular studies of DivIVA dynamics, biophysical studies of DivIVA interaction with the membrane, as well as high-resolution structural studies in the cell, such as cryo-correlative light and electron microscopy (cryo-CLEM), to correlate the localization of DivIVA with the architecture of cellular ultrastructures.

MATERIALS AND METHODS

Bacterial strains and growth conditions

The pneumococcal strains used in this study are listed in Table S1. For PG labeling, 50 µL of glycerol stocks, frozen at OD_{600nm} = 0.3, was used to inoculate 1 mL of BHI medium. Cultures were grown at 37°C in a static CO_2 incubator, diluted twice into 10 mL of pre-warmed BHI medium (1/10th volume) to reach steady-state growth, and treated for PG labeling when OD_{600nm} reached 0.3.

To localize DivIVA, cultures were inoculated at OD_{600nm} = 0.006 in C + Y medium and grown at 37°C to an OD_{600nm} of 0.3. These cultures were diluted into C + Y medium (1/50th volume) and incubated at 37°C to an OD_{600nm} of 0.1. The cells were then incubated 10 min at 37°C with 20 nM HT-JFX646 ligand. For STED Microscopy, to fix the cells, 300 µL of culture was mixed with 100 µL of fixation solution (0.5 M KPO_4 pH 7, 8% paraformaldehyde, 0.08% glutaraldehyde) and incubated for 15 min at room temperature followed by 15 min on ice. Cells were then washed twice with 300 µL

of 0.1 M KPO_4 and finally concentrated three times. 0.8 µL of the cell suspension was immobilized on a 1.2% C + Y agarose-coated microscopy slide with a cover glass (# 1.5) for cell imaging.

Strain constructions

Strain R4596, containing a *divIVA-HaloTag* fusion at the *divIVA* endogeneous locus, was generated as follows. Primers were designed to amplify PCR products containing: (i) the upstream region and the entire coding sequence of the *divIVA* (*spr1505*) gene (2,234 bp; oligonucleotides DJ8 and DJ43, and R1501 DNA as template); (ii) a 12 amino-acid linker, L5 (17, 43), and the *orf* encoding the HaloTag sequence (982 bp; oligonucleotides DJ41 and DJ42, and a DNA fragment containing the HaloTag sequence generated by Integrated DNA Technologies); and (iii) the downstream region of the *divIVA* gene (2,062 bp; oligonucleotides DJ44 and DJ10, and R1501 DNA as template). The PCR products were gel-purified and used as templates in an SOEing PCR using the outer primers DJ8 and DJ10. The resulting SOEing PCR product was subsequently used to transform strain R1501 without selection, as previously described (57).

Epifluorescence and STED microscopy

Epifluorescence snapshots were performed on a Nikon Ti-E Eclipse microscope, equipped with a 100× objective as previously described (58). The 561 nm excitation laser was set at 30% of the maximum excitation power with an exposure time of 500 ms. Demographs showing the fluorescence intensity of DivIVA relative to cell length were generated using MicrobeJ (version 5.13 n), with specific parameters as previously reported (59): area (0.6–20 µm^2), length (0.5-max µm), width (0.5–2 µm), circularity (0–1), curvature (0-max), sinuosity (0-max), angularity (0–0.25 rad), solidity (0–0.85 max), and intensity (0-max). Cells with regular morphology that were initially excluded from the segmentation due to close proximity to other cells were manually re-included in the analysis. Adjacent ovoid cells were meticulously examined to ensure accurate classification as one late-division cell or two separated daughter cells. The resulting data were normalized as per MicrobeJ's guidelines. Heatmaps illustrating the average fluorescence intensity of DivIVA-HT (Fig. 1B) were generated with MicrobeJ, using cell categorization parameters as follows from left to right: [SHAPE.length] ≤ 1.277; [SHAPE.length] > 1.277 and [SHAPE.length] ≤ 1.577; [SHAPE.length] > 1.577 and [SHAPE.length] ≤ 2.245; [SHAPE.length] > 2.245. Within these segmented cells, ROIs were manually selected using the FIJI package to quantify the average fluorescence intensity at the septum and at the cell poles (Fig. 1C).

STED microscopy images were acquired with a STEDYCON system (Abberior Instruments GmbH). Pulsed laser at 640 nm was used for fluorescence excitation. A pulsed 775 nm STED depletion laser was additionally used. The 640 nm excitation laser and the 775 nm depletion laser were set at 10% of their maximum power. The optical setup was connected to an AxioImager Z2 fluorescence microscope (Zeiss) with a 100 × oil immersion PlanApochromat objective lens (NA = 1.46). The acquisition software was STEDYCON Smart control. Measurements were performed with a pixel dwell time of 10 µs.

Preparation of PG labeling reagents

All starting materials were obtained from commercial sources and were used without further purification. NMR spectra were acquired on a Bruker Advance 400 MHz for ^{1}H-NMR experiments and 100 MHz for ^{13}C-NMR experiments. Chemical shifts are reported in ppm (δ) relative to the solvents: ^{1}H $\delta(CD_3OD)$ = 3.3 ppm, ^{13}C $\delta(CD_3OD)$ = 49.15 ppm. Accurate mass spectra were recorded on a time-of-flight (TOF) spectrometer (Waters, XEVO G2-S QTof) and on an LTQ Orbitrap XL spectrometer with ElectroSpay Ionization (ESI, Thermo Scientific).

The aDA-DA probe (((*R*)–2-amino-3-azidopropanoyl)-D-alanine) was synthesized as previously described (3). Briefly, 2-(trimethylsilyl)ethyl (*tert*-butoxycarbonyl)-D-alaninate

was obtained according to the Van Nieuwenhze's process and the (*R*)-3-azido-2-((*tert*-butoxycarbonyl)amino)propanoic acid was obtained according to the Webb's process (described for the L enantiomer) (60, 61).

The N-Boc deprotection of 2-(trimethylsilyl)ethyl (*tert*-butoxycarbonyl)-D-alaninate was performed in a solution of 4 N HCl in dioxane for 3 h to give, after removal of solvent, trituration in dried ether, and drying under high vacuum (4 h), the corresponding salt in quantitative yield. This latter and the (*R*)-3-azido-2-((*tert*-butoxycarbonyl)amino)propanoic acid (1.4 equivalent) were dissolved in dry CH_2Cl_2. HATU (1.1 equivalent), di-isopropyl ethyl amine (DIPEA, 2.3 equivalent) was added, and the mixture was stirred overnight. After removal of the solvent, ethyl acetate was added and the solution was washed with an aqueous solution of 10% citric acid followed by 5% $NaHCO_3$. The combined organic layers were dried ($MgSO_4$) and evaporated. After purification flash chromatography, the resulting 2-(trimethylsilyl)ethyl ((*R*)-3-azido-2-((*ter*-butoxycarbonyl)amino)propanoyl)-D-alaninate was obtained in 63% yield. The final deprotections were performed by the addition of trifluoroacetic acid (TFA) at 0°C followed by stirring for 4 h at room temperature. The solvent was evaporated and dried under a high vacuum (oil pump). The compound was purified by HPLC to yield ((*R*)-2-ammonio-3-azidopropanoyl)-D-alaninate 2,2,2-trifluoroacetate (aDADA) as a white solid.

Frozen aliquots of a 500 mM stock solution of aDA-DA in 100% DMSO were diluted to 10 mM in commercial DPBS (calcium- and magnesium-free, from ThermoFisher) and stored at −20°C for subsequent use.

Powder of DBCO-AF647 (Jena Bioscience) was resuspended at 10 mM into 100% DMSO, diluted to 500 µM into DPBS, and stored at −20°C for subsequent use.

PG labeling in *S. pneumoniae* cells

Cells in the exponential growth phase (OD_{600nm} 0.3) were incubated for 5 min at 37°C in a BHI medium containing 2 mM aDA-DA (PULSE labeling). For PULSE-CHASE labeling experiments, after the 5 min PULSE labeling with aDA-DA, cells were pelleted (7,000 × *g*, 5 min, 20°C) and resuspended into fresh, pre-warmed BHI medium. Incubation at 37°C was continued for 15 min. Following PULSE or PULSE-CHASE labeling, cells were fixed overnight on ice, in the culture medium supplemented with 0.5× DPBS and 2% (vol/vol) paraformaldehyde (PFA). Following fixation, cells were pelleted, resuspended into DPBS containing 35 µM DBCO-AF647, and incubated for 1 h at 20°C (click reaction). Cells were then washed twice with 1 mL of DPBS and were resuspended into the dSTORM buffer, which contains 25 mM NaCl, 75 mM Tris-HCl pH 8.0, 10% (wt/vol) D-glucose, 100 mM cysteamine (β-mercaptoethylamine), and 1× GLOX mix [40 µg·mL^{-1} catalase from bovine liver (Sigma-Aldrich), 0.5 mg·mL^{-1} glucose oxidase type VII from *Aspergillus niger* (Sigma-Aldrich)]. Further details regarding the labeling procedure and alternative strategies can be found in reference (30).

dSTORM data acquisition

To perform dSTORM on cells oriented along their longitudinal axis, the samples were mounted between a slide (High-precision, No. 1.5H, 24 × 50 mm, 170 ± 5 mm, Marienfeld) and a coverslip (High-precision, No. 1.5H, 22 × 22 mm, 170 ± 5 µm, Marienfeld) previously treated with ozone and eventually sealed with colorless nail polish.

To orient cells with a tilt angle, 8 µL of sample was loaded on a slide and covered with 18 µL of dSTORM buffer containing 0.9% (wt/vol) low-melting agarose. The slide was then turned over onto a coverslip. After solidification, the agarose pad was sealed with colorless nail polish.

dSTORM images were acquired at 27°C with a SAFe360 Abbelight PALM/STORM setup based on an Olympus IX83 inverted microscope equipped with a Oxxius laser combiner and two sCMOS Hamamatsu ORCA-Fusion cameras controlled via the NEO software. The emitted signal was collected by a 100× oil immersion apochromatic objective (UPLAPO100XOHR, Olympus) and then filtered by a band-pass filter FF01-698/70 (Semrock). First, diffraction-limited images were acquired by illuminating the sample at

640 nm with 1% of the maximal laser power (2 kW·cm^{-2}). For single-molecule localization microscopy, the samples were exposed to a continuous 640 nm illumination with a constant laser power density of 2 kW·cm^{-2}. dSTORM data were collected over 15,000 frames recorded with an exposure time of 50 ms. The blinking density was maintained all along the data collection by ramping up a 405 nm laser from 0% to 15% of a maximal value of 50 W·cm^{-2} For homogenous excitation of the sample, the field of excitation parameter in the NEO software was adjusted to cover the region of interest (ASTER illumination) (62).

dSTORM image reconstruction

Data processing was performed with the ThunderSTORM plugin in ImageJ/FIJI (63–65), including the determination of the localization precision and quantification of the number of localizations. Potential drift was corrected with the cross-correlation tool in ThunderSTORM (63). Image rendering was achieved through normalized Gaussian blurring with a reconstructed pixel size of 10 nm. The spatial resolution of the reconstructed dSTORM images was calculated using the FIRE ImageJ/FIJI plugin (66). Further details for dSTORM data acquisition and image reconstruction can be found in reference (30).

Measurement of the labeling patterns

Measurements of the labeled regions were performed in ImageJ (64). The values of the diameter d and of the width of the chase W_{CHASE} (as defined in Fig. 2C and 5B) were obtained by plotting the signal intensity along a line positioned over the labeling of interest and measuring the distance between the points at half the maximal intensity.

For radial labeling patterns (in vertical or angled bacteria), the diameters d_{out} and d_{in} are used to calculate the radial thickness r of the labeled region, as defined in Fig. 4B, were measured as above along a line positioned across the longest axis of the elliptic patterns.

Geometrical model of cell growth and labeling

The basis of the geometrical model was similar to that developed previously for WT strains (3). The animated geometrical model was implemented using the free open source 3D animation software Art of Illusion© by Peter Eastman. The mature cell was modeled as an ellipsoid of length L and diameter D. Taking the longitudinal axis as the x axis, the equator as its origin, and L the length of a mature single cell, the radius of the cell around this axis (R_{out}) is given by the elliptic curve:

$$R_{out(x)} = \sqrt{y_{out}^2 + z_{out}^2} = \sqrt{1 - \left(\frac{x}{L/2}\right)^2}$$

Taking l as the distance between two parting equators, as the new cell length $l/2$ grows along x with time, R_{out} at $x = l/2$ is the radius of the septal outer edge circle ($R_{out} = d_{out}/2$). Taking the length C, at which the septum is closed, the radius of the septal inner edge circle ($R_{in} = d_{in}/2$) at $x = l/2$ is given by

$$R_{in(x)} = \sqrt{y_{in}^2 + z_{in}^2} = \sqrt{1 - \left(\frac{x}{C/2}\right)^2}$$

That points on the inner septal edge follow an elliptic path toward the point of closure is an assumption that was found to match the observations of the WT strains. We have set $R_{max} = D/2 = 1$ so that in the above equations, $L/2$ takes the numerical value of the elliptic factor $E = L/D$.

To account for the acceleration of the growth along the x axis observed in WT strains, $l/2$ depends on time according to:

$$l/2_{(t)} = \frac{(1 + At)}{2\,(1 + A)}$$

where A is an acceleration factor. Note that in this equation, t and A are dimensionless and t is expressed as a fraction of the generation time, which is defined as 1. The $(1 + A)$ denominator is a normalization factor that ensures that a division is completed at $t = 1$.

Since the acceleration was not observed in the *ΔdivIVA* strain, A was set to 0 to describe the deletion phenotype. Instead, three additional parameters were introduced in the model. A time point after the initiation of the division at which the cell elongation slows down (T_s), and the factor by which the elongation rate is diminished ("brake" factor B). When B is set to 1, growth continues unchanged after T_s at the normalized rate of 1 and the division cycle is completed at $t = 1$. If B is set as a fraction of 1, the cell elongation continues at rate B after T_s, and the division ends at $t = T_s + (1-T_s)/B$, which is greater than 1.

$$l/2_{(t < T_s)} =$$
$$l/2_{(t > T_s)} = LT_s + BL(t - T_s)$$

The third parameter that was added determines a point at which all processes stop. For practical reason of programming in Art of Illusion©, this event was defined as a fraction (S) of the length that the cell would have attained without growth arrest, rather than as a time.

The start and length of the labeling pulse can also be defined. In contrast to the WT strains, where the evolution of the various distances (length l, inner and outer septal diameter d_{in} and d_{out} could be fitted to measurements to extract values of the model parameters, the parameter describing the *ΔdivIVA* strain were manually adjusted to best reproduce the observations, due to the greater heterogeneity of the cell sizes and morphologies. Nevertheless, all the simulated labeling patterns presented were generated with the same set of parameters, which are given in Table 1.

Quantification and statistical analysis

Statistics were performed using Excel, and figures were prepared using LabPlot2. The statistical details describing the quantification and measurements of localization patterns (including the definition of center, dispersion and precision of measures, the statistical tests used, the exact value of the n number of analyzed cells) can be found in the Results section and in the figure legends.

ACKNOWLEDGMENTS

We thank members of the Morlot and Grangeasse laboratories for advice and encouragement, O. Glushonkov and J.P. Kleman for advices and support regarding dSTORM. Support for this work comes from the Agence Nationale de la Recherche (ANR-16-CE11-0016 and ANR-23-CE11-0029 to C.M., ANR-19-CE15-0011 to C.G., Labex ARCANE ANR-17-EURE-0003 to Y.S.W., and ANR-17-CE13-0031 to R.C.L. and N.C.), from the European Research Council (ERC) under the Horizon 2020 research and innovation program (grant agreement No 772178 to R.C.L.), and from a fellowship "Fin de thèse" of the Fondation pour la Recherche Médicale (FDT202204014744 to D.J.). This work used the platforms of the Grenoble Instruct-ERIC centre (ISBG; UMS 3518 CNRS-CEA-UGA-EMBL) within the Grenoble Partnership for Structural Biology (PSB), supported by FRISBI (ANR-10-INBS-05-02) and GRAL, financed within the University Grenoble Alpes graduate school (Ecoles Universitaires de Recherche) CBH-EUR-GS (ANR-17-EURE-0003). I.B.S. acknowledges integration into the Interdisciplinary Research Institute of Grenoble (IRIG, CEA).

J.T., A.Z., R.C.L., N.C., Y.S.W., C.G., and C.M. designed research; J.T., A.Z., L.B., D.J., A.P., C.F., and M.B. performed experiments; J.T., A.Z., D.J., N.C., Y.S.W., C.G., and C.M. analyzed

data; J.T., A.Z., and C.M. wrote the manuscript; J.T., A.Z., R.C.L., N.C., Y.S.W., C.G., and C.M. revised the manuscript.

While citing references scientifically relevant for this work, we also actively worked to promote gender balance in our reference list.

AUTHOR AFFILIATIONS

[1]Université Grenoble Alpes, CNRS, CEA, IBS, Grenoble, France
[2]Université Paris-Saclay, INRAE, AgroParisTech, Micalis Institute, Jouy-en-Josas, France
[3]Molecular Microbiology and Structural Biochemistry (MMSB), CNRS, Université Lyon 1, UMR 5086, Lyon, France
[4]Université Grenoble Alpes, CNRS, DPM, Grenoble, France
[5]Laboratoire de Microbiologie et Génétique Moléculaires, UMR 5100, Centre de Biologie Intégrative, Centre National de la Recherche Scientifique, Toulouse, France
[6]Université Paul Sabatier (Toulouse III), Toulouse, France

AUTHOR ORCIDs

Rut Carballido-Lopez http://orcid.org/0000-0001-9383-8811
Cecile Morlot http://orcid.org/0000-0002-9295-1035

FUNDING

Funder	Grant(s)	Author(s)
Agence Nationale de la Recherche (ANR)	ANR-16-CE11-0016	Cecile Morlot
Agence Nationale de la Recherche (ANR)	ANR-23-CE11-0029	Cecile Morlot
Agence Nationale de la Recherche (ANR)	ANR-19-CE15-0011	Christophe Grangeasse
Agence Nationale de la Recherche (ANR)	Labex ARCANE ANR-17-EURE-0003	Yung-Sing Wong
Agence Nationale de la Recherche (ANR)	ANR-17-CE13-0031	Rut Carballido-Lopez
EC | European Research Council (ERC)	No 772178	Rut Carballido-Lopez
Fondation pour la Recherche Médicale (FRM)	FDT202204014744	Dimitri Juillot

AUTHOR CONTRIBUTIONS

Jennyfer Trouve, Data curation, Formal analysis, Investigation, Methodology, Visualization, Writing – original draft, Writing – review and editing | André Zapun, Data curation, Formal analysis, Investigation, Methodology, Software, Validation, Visualization, Writing – original draft, Writing – review and editing | Laure Bellard, Formal analysis, Investigation, Visualization | Dimitri Juillot, Formal analysis, Investigation, Visualization, Writing – review and editing | Anais Pelletier, Investigation, Visualization | Celine Freton, Investigation, Visualization | Morgane Baudoin, Formal analysis, Investigation | Rut Carballido-Lopez, Conceptualization, Data curation, Formal analysis, Funding acquisition, Methodology, Resources, Supervision, Validation, Visualization, Writing – review and editing | Nathalie Campo, Conceptualization, Data curation, Formal analysis, Funding acquisition, Investigation, Methodology, Resources, Supervision, Validation, Visualization, Writing – review and editing | Yung-Sing Wong, Conceptualization, Formal analysis, Funding acquisition, Methodology, Resources, Supervision, Validation, Writing – review and editing | Christophe Grangeasse, Conceptualization, Formal analysis, Funding acquisition, Resources, Supervision, Validation, Visualization, Writing – review and editing | Cecile Morlot, Conceptualization, Data curation, Formal analysis, Funding acquisition,

Investigation, Methodology, Project administration, Resources, Supervision, Validation, Visualization, Writing – original draft, Writing – review and editing

DATA AVAILABILITY

There are restrictions to the availability of the aDA-DA probe. Due to the time required for chemical synthesis, this material will be available through a collaboration with Yung-Sing Wong (yung-sing.wong@univ-grenoble-alpes.fr).
The data sets generated during this study are available on the Zenodo platform [https://doi.org/10.5281/zenodo.13270454].

ADDITIONAL FILES

The following material is available online.

Supplemental Material

Supplemental material (mBio01311-24-s0001.docx). Fig. S1 to S5 and Tables S1 and S2.

REFERENCES

1. Vollmer W, Blanot D, de Pedro MA. 2008. Peptidoglycan structure and architecture. FEMS Microbiol Rev 32:149–167. https://doi.org/10.1111/j.1574-6976.2007.00094.x
2. Pinho MG, Kjos M, Veening J-W. 2013. How to get (a)round: mechanisms controlling growth and division of coccoid bacteria. Nat Rev Microbiol 11:601–614. https://doi.org/10.1038/nrmicro3088
3. Trouve J, Zapun A, Arthaud C, Durmort C, Di Guilmi AM, Söderström B, Pelletier A, Grangeasse C, Bourgeois D, Wong Y-S, Morlot C. 2021. Nanoscale dynamics of peptidoglycan assembly during the cell cycle of *Streptococcus pneumoniae*. Curr Biol 31:2844–2856. https://doi.org/10.1016/j.cub.2021.04.041
4. Meeske AJ, Riley EP, Robins WP, Uehara T, Mekalanos JJ, Kahne D, Walker S, Kruse AC, Bernhardt TG, Rudner DZ. 2016. SEDS proteins are a widespread family of bacterial cell wall polymerases. Nature New Biol 537:634–638. https://doi.org/10.1038/nature19331
5. Sauvage E, Kerff F, Terrak M, Ayala JA, Charlier P. 2008. The penicillin-binding proteins: structure and role in peptidoglycan biosynthesis. FEMS Microbiol Rev 32:234–258. https://doi.org/10.1111/j.1574-6976.2008.00105.x
6. Käshammer L, van den Ent F, Jeffery M, Jean NL, Hale VL, Löwe J. 2023. Cryo-EM structure of the bacterial divisome core complex and antibiotic target FtsWIQBL. Nat Microbiol 8:1149–1159. https://doi.org/10.1038/s41564-023-01368-0
7. Reichmann NT, Tavares AC, Saraiva BM, Jousselin A, Reed P, Pereira AR, Monteiro JM, Sobral RG, VanNieuwenhze MS, Fernandes F, Pinho MG. 2019. SEDS-bPBP pairs direct lateral and septal peptidoglycan synthesis in *Staphylococcus aureus*. Nat Microbiol 4:1368–1377. https://doi.org/10.1038/s41564-019-0437-2
8. Sjodt M, Rohs PDA, Gilman MSA, Erlandson SC, Zheng S, Green AG, Brock KP, Taguchi A, Kahne D, Walker S, Marks DS, Rudner DZ, Bernhardt TG, Kruse AC. 2020. Structural coordination of polymerization and crosslinking by a SEDS-bPBP peptidoglycan synthase complex. Nat Microbiol 5:813–820. https://doi.org/10.1038/s41564-020-0687-z
9. Taguchi A, Welsh MA, Marmont LS, Lee W, Sjodt M, Kruse AC, Kahne D, Bernhardt TG, Walker S. 2019. FtsW is a peptidoglycan polymerase that is functional only in complex with its cognate penicillin-binding protein. Nat Microbiol 4:587–594. https://doi.org/10.1038/s41564-018-0345-x
10. Zapun A, Noirclerc-Savoye M, Helassa N, Vernet T. 2012. Peptidoglycan assembly machines: the biochemical evidence. Microb Drug Resist 18:256–260. https://doi.org/10.1089/mdr.2011.0236
11. Cho H, Wivagg CN, Kapoor M, Barry Z, Rohs PDA, Suh H, Marto JA, Garner EC, Bernhardt TG. 2016. Bacterial cell wall biogenesis is mediated by SEDS and PBP polymerase families functioning semi-autonomously. Nat Microbiol 1:16172. https://doi.org/10.1038/nmicrobiol.2016.172
12. Straume D, Piechowiak KW, Kjos M, Håvarstein LS. 2021. Class A PBPs: it is time to rethink traditional paradigms. Mol Microbiol 116:41–52. https://doi.org/10.1111/mmi.14714
13. Vigouroux A, Cordier B, Aristov A, Alvarez L, Özbaykal G, Chaze T, Oldewurtel ER, Matondo M, Cava F, Bikard D, van Teeffelen S. 2020. Class-A penicillin binding proteins do not contribute to cell shape but repair cell-wall defects. Elife 9:e51998. https://doi.org/10.7554/eLife.51998
14. Vollmer W, Joris B, Charlier P, Foster S. 2008. Bacterial peptidoglycan (murein) hydrolases. FEMS Microbiol Rev 32:259–286. https://doi.org/10.1111/j.1574-6976.2007.00099.x
15. Briggs NS, Bruce KE, Naskar S, Winkler ME, Roper DI. 2021. The pneumococcal divisome: dynamic control of *Streptococcus pneumoniae* cell division. Front Microbiol 12:737396. https://doi.org/10.3389/fmicb.2021.737396
16. Zapun A, Vernet T, Pinho MG. 2008. The different shapes of cocci. FEMS Microbiol Rev 32:345–360. https://doi.org/10.1111/j.1574-6976.2007.00098.x
17. Perez AJ, Cesbron Y, Shaw SL, Bazan Villicana J, Tsui H-C, Boersma MJ, Ye ZA, Tovpeko Y, Dekker C, Holden S, Winkler ME. 2019. Movement dynamics of divisome proteins and PBP2x:FtsW in cells of *Streptococcus pneumoniae*. Proc Natl Acad Sci U S A 116:3211–3220. https://doi.org/10.1073/pnas.1816018116
18. Philippe J, Vernet T, Zapun A. 2014. The elongation of ovococci. Microb Drug Resist 20:215–221. https://doi.org/10.1089/mdr.2014.0032
19. Straume D, Stamsås GA, Berg KH, Salehian Z, Håvarstein LS. 2017. Identification of pneumococcal proteins that are functionally linked to penicillin-binding protein 2b (PBP2b). Mol Microbiol 103:99–116. https://doi.org/10.1111/mmi.13543
20. Paik J, Kern I, Lurz R, Hakenbeck R. 1999. Mutational analysis of the *Streptococcus pneumoniae* bimodular class A penicillin-binding proteins. J Bacteriol 181:3852–3856. https://doi.org/10.1128/JB.181.12.3852-3856.1999
21. Straume D, Piechowiak KW, Olsen S, Stamsås GA, Berg KH, Kjos M, Heggenhougen MV, Alcorlo M, Hermoso JA, Håvarstein LS. 2020. Class A PBPs have a distinct and unique role in the construction of the pneumococcal cell wall. Proc Natl Acad Sci U S A 117:6129–6138. https://doi.org/10.1073/pnas.1917820117
22. Bai X-H, Chen H-J, Jiang Y-L, Wen Z, Huang Y, Cheng W, Li Q, Qi L, Zhang J-R, Chen Y, Zhou C-Z. 2014. Structure of pneumococcal peptidoglycan hydrolase LytB reveals insights into the bacterial cell wall remodeling and pathogenesis. J Biol Chem 289:23403–23416. https://doi.org/10.1074/jbc.M114.579714
23. Barendt SM, Land AD, Sham L-T, Ng W-L, Tsui H-C, Arnold RJ, Winkler ME. 2009. Influences of capsule on cell shape and chain formation of wild-type and *pcsB* mutants of serotype 2 *Streptococcus pneumoniae*. J Bacteriol 191:3024–3040. https://doi.org/10.1128/JB.01505-08
24. Bartual SG, Straume D, Stamsås GA, Muñoz IG, Alfonso C, Martínez-Ripoll M, Håvarstein LS, Hermoso JA. 2014. Structural basis of PcsB-mediated

cell separation in *Streptococcus pneumoniae*. Nat Commun 5:3842. https://doi.org/10.1038/ncomms4842
25. De Las Rivas B, García JL, López R, García P. 2002. Purification and polar localization of pneumococcal LytB, a putative endo-beta-N-acetylglucosaminidase: the chain-dispersing murein hydrolase. J Bacteriol 184:4988–5000. https://doi.org/10.1128/JB.184.18.4988-5000.2002
26. Jacq M, Arthaud C, Manuse S, Mercy C, Bellard L, Peters K, Gallet B, Galindo J, Doan T, Vollmer W, Brun YV, VanNieuwenhze MS, Di Guilmi AM, Vernet T, Grangeasse C, Morlot C. 2018. The cell wall hydrolase Pmp23 is important for assembly and stability of the division ring in *Streptococcus pneumoniae*. Sci Rep 8:7591. https://doi.org/10.1038/s41598-018-25882-y
27. Taguchi A, Page JE, Tsui H-C, Winkler ME, Walker S. 2021. Biochemical reconstitution defines new functions for membrane-bound glycosidases in assembly of the bacterial cell wall. Proc Natl Acad Sci U S A 118:e2103740118. https://doi.org/10.1073/pnas.2103740118
28. Tsui H-CT, Zheng JJ, Magallon AN, Ryan JD, Yunck R, Rued BE, Bernhardt TG, Winkler ME. 2016. Suppression of a deletion mutation in the gene encoding essential PBP2b reveals a new lytic transglycosylase involved in peripheral peptidoglycan synthesis in *Streptococcus pneumoniae* D39. Mol Microbiol 100:1039–1065. https://doi.org/10.1111/mmi.13366
29. Schermelleh L, Ferrand A, Huser T, Eggeling C, Sauer M, Biehlmaier O, Drummen GPC. 2019. Super-resolution microscopy demystified. Nat Cell Biol 21:72–84. https://doi.org/10.1038/s41556-018-0251-8
30. Trouve J, Glushonkov O, Morlot C. 2021. Metabolic biorthogonal labeling and dSTORM imaging of peptidoglycan synthesis in *Streptococcus pneumoniae* STAR Protoc 2:101006. https://doi.org/10.1016/j.xpro.2021.101006
31. Jacq M, Adam V, Bourgeois D, Moriscot C, Di Guilmi A-M, Vernet T, Morlot C. 2015. Remodeling of the Z-ring nanostructure during the *Streptococcus pneumoniae* cell cycle revealed by photoactivated localization microscopy. MBio 6:e01108-15. https://doi.org/10.1128/mBio.01108-15
32. Perez AJ, Boersma MJ, Bruce KE, Lamanna MM, Shaw SL, Tsui H-C, Taguchi A, Carlson EE, VanNieuwenhze MS, Winkler ME. 2021. Organization of peptidoglycan synthesis in nodes and separate rings at different stages of cell division of *Streptococcus pneumoniae*. Mol Microbiol 115:1152–1169. https://doi.org/10.1111/mmi.14659
33. Hammond LR, White ML, Eswara PJ. 2019. ¡vIVA la DivIVA! J Bacteriol 201:e00245-19. https://doi.org/10.1128/JB.00245-19
34. Halbedel S, Lewis RJ. 2019. Structural basis for interaction of DivIVA/GpsB proteins with their ligands. Mol Microbiol 111:1404–1415. https://doi.org/10.1111/mmi.14244
35. Fadda D, Santona A, D'Ulisse V, Ghelardini P, Ennas MG, Whalen MB, Massidda O. 2007. *Streptococcus pneumoniae* DivIVA: localization and interactions in a MinCD-free context. J Bacteriol 189:1288–1298. https://doi.org/10.1128/JB.01168-06
36. Fleurie A, Manuse S, Zhao C, Campo N, Cluzel C, Lavergne J-P, Freton C, Combet C, Guiral S, Soufi B, Macek B, Kuru E, VanNieuwenhze MS, Brun YV, Di Guilmi A-M, Claverys J-P, Galinier A, Grangeasse C. 2014. Interplay of the serine/threonine-kinase StkP and the paralogs DivIVA and GpsB in pneumococcal cell elongation and division. PLOS Genet 10:e1004275. https://doi.org/10.1371/journal.pgen.1004275
37. Fadda D, Pischedda C, Caldara F, Whalen MB, Anderluzzi D, Domenici E, Massidda O. 2003. Characterization of *divIVA* and other genes located in the chromosomal region downstream of the *dcw* cluster in *Streptococcus pneumoniae*. J Bacteriol 185:6209–6214. https://doi.org/10.1128/JB.185.20.6209-6214.2003
38. Jiang Q, Li B, Zhang L, Li T, Hu Q, Li H, Zou W, Hu Z, Huang Q, Zhou R. 2023. DivIVA interacts with the cell wall hydrolase MltG to regulate peptidoglycan synthesis in *Streptococcus suis*. Microbiol Spectr 11:e0475022. https://doi.org/10.1128/spectrum.04750-22
39. Cramer K, Reinhardt SCM, Auer A, Shin JY, Jungmann R. 2024. Comparing divisome organization between vegetative and sporulating *Bacillus subtilis* at the nanoscale using DNA-PAINT. Sci Adv 10:eadk5847. https://doi.org/10.1126/sciadv.adk5847
40. Lenarcic R, Halbedel S, Visser L, Shaw M, Wu LJ, Errington J, Marenduzzo D, Hamoen LW. 2009. Localisation of DivIVA by targeting to negatively curved membranes. EMBO J 28:2272–2282. https://doi.org/10.1038/emboj.2009.129
41. Sutton JAF, Cooke M, Tinajero-Trejo M, Wacnik K, Salamaga B, Portman-Ross C, Lund VA, Hobbs JK, Foster SJ. 2023. The roles of GpsB and DivIVA in *Staphylococcus aureus* growth and division. Front Microbiol 14:1241249. https://doi.org/10.3389/fmicb.2023.1241249
42. Los GV, Encell LP, McDougall MG, Hartzell DD, Karassina N, Zimprich C, Wood MG, Learish R, Ohana RF, Urh M, Simpson D, Mendez J, Zimmerman K, Otto P, Vidugiris G, Zhu J, Darzins A, Klaubert DH, Bulleit RF, Wood KV. 2008. HaloTag: a novel protein labeling technology for cell imaging and protein analysis. ACS Chem Biol 3:373–382. https://doi.org/10.1021/cb800025k
43. van Raaphorst R, Kjos M, Veening J-W. 2017. Chromosome segregation drives division site selection in *Streptococcus pneumoniae*. Proc Natl Acad Sci U S A 114:E5959–E5968. https://doi.org/10.1073/pnas.1620608114
44. Eswaramoorthy P, Erb ML, Gregory JA, Silverman J, Pogliano K, Pogliano J, Ramamurthi KS. 2011. Cellular architecture mediates DivIVA ultrastructure and regulates min activity in *Bacillus subtilis*. MBio 2:e00257-11. https://doi.org/10.1128/mBio.00257-11
45. Feddersen H, Würthner L, Frey E, Bramkamp M. 2021. Dynamics of the *Bacillus subtilis* min system. MBio 12:e00296-21. https://doi.org/10.1128/mBio.00296-21
46. Vollmer W, Massidda O, Tomasz A. 2019. The cell wall of *Streptococcus pneumoniae*. Microbiol Spectr 7. https://doi.org/10.1128/microbiolspec.GPP3-0018-2018
47. Choukate K, Chaudhuri B. 2020. Structural basis of self-assembly in the lipid-binding domain of mycobacterial polar growth factor Wag31. IUCrJ 7:767–776. https://doi.org/10.1107/S2052252520006053
48. Oliva MA, Halbedel S, Freund SM, Dutow P, Leonard TA, Veprintsev DB, Hamoen LW, Löwe J. 2010. Features critical for membrane binding revealed by DivIVA crystal structure. EMBO J 29:1988–2001. https://doi.org/10.1038/emboj.2010.99
49. Ramamurthi KS, Losick R. 2009. Negative membrane curvature as a cue for subcellular localization of a bacterial protein. Proc Natl Acad Sci U S A 106:13541–13545. https://doi.org/10.1073/pnas.0906851106
50. Kang C-M, Nyayapathy S, Lee J-Y, Suh J-W, Husson RN. 2008. Wag31, a homologue of the cell division protein DivIVA, regulates growth, morphology and polar cell wall synthesis in mycobacteria. Microbiol Read Engl 154:725–735. https://doi.org/10.1099/mic.0.2007/014076-0
51. Letek M, Ordóñez E, Vaquera J, Margolin W, Flärdh K, Mateos LM, Gil JA. 2008. DivIVA is required for polar growth in the MreB-lacking rod-shaped actinomycete *Corynebacterium glutamicum*. J Bacteriol 190:3283–3292. https://doi.org/10.1128/JB.01934-07
52. Edwards DH, Errington J. 1997. The *Bacillus subtilis* DivIVA protein targets to the division septum and controls the site specificity of cell division. Mol Microbiol 24:905–915. https://doi.org/10.1046/j.1365-2958.1997.3811764.x
53. Giacomelli G, Feddersen H, Peng F, Martins GB, Grafemeyer M, Meyer F, Mayer B, Graumann PL, Bramkamp M. 2022. Subcellular dynamics of a conserved bacterial polar scaffold protein. Genes (Basel) 13:278. https://doi.org/10.3390/genes13020278
54. Berg KH, Stamsås GA, Straume D, Håvarstein LS. 2013. Effects of low PBP2b levels on cell morphology and peptidoglycan composition in *Streptococcus pneumoniae* R6. J Bacteriol 195:4342–4354. https://doi.org/10.1128/JB.00184-13
55. Messelink JJ, Meyer F, Bramkamp M, Broedersz CP. 2021. Single-cell growth inference of *Corynebacterium glutamicum* reveals asymptotically linear growth. Elife 10:e70106. https://doi.org/10.7554/eLife.70106
56. Sieger B, Bramkamp M. 2014. Interaction sites of DivIVA and RodA from *Corynebacterium glutamicum*. Front Microbiol 5:738. https://doi.org/10.3389/fmicb.2014.00738
57. Quevillon-Cheruel S, Campo N, Mirouze N, Mortier-Barrière I, Brooks MA, Boudes M, Durand D, Soulet A-L, Lisboa J, Noirot P, Martin B, van Tilbeurgh H, Noirot-Gros M-F, Claverys J-P, Polard P. 2012. Structure-function analysis of pneumococcal DprA protein reveals that dimerization is crucial for loading RecA recombinase onto DNA during transformation. Proc Natl Acad Sci U S A 109:E2466–E2475. https://doi.org/10.1073/pnas.1205638109
58. Billaudeau C, Chastanet A, Yao Z, Cornilleau C, Mirouze N, Fromion V, Carballido-López R. 2017. Contrasting mechanisms of growth in two model rod-shaped bacteria. Nat Commun 8:15370. https://doi.org/10.1038/ncomms15370

59. Juillot D, Billaudeau C, Barbotin A, Lablaine A, Mortier-Barrière I, Polard P, Campo N, Carballido-Lopez R. 2024. Transient inhibition of cell division in competent pneumococcal cells results from deceleration of the septal peptidoglycan complex. bioRxiv. https://doi.org/10.1101/2024.02.28.582556
60. Liechti GW, Kuru E, Hall E, Kalinda A, Brun YV, VanNieuwenhze M, Maurelli AT. 2014. A new metabolic cell-wall labelling method reveals peptidoglycan in *Chlamydia trachomatis*. Nature New Biol 506:507–510. https://doi.org/10.1038/nature12892
61. McAllister TE, Nix MG, Webb ME. 2011. Fmoc-chemistry of a stable phosphohistidine analogue. Chem Commun 47:1297–1299. https://doi.org/10.1039/C0CC04238B
62. Mau A, Friedl K, Leterrier C, Bourg N, Lévêque-Fort S. 2021. Fast widefield scan provides tunable and uniform illumination optimizing super-resolution microscopy on large fields. Nat Commun 12:3077. https://doi.org/10.1038/s41467-021-23405-4
63. Ovesný M, Křížek P, Borkovec J, Švindrych Z, Hagen GM. 2014. ThunderSTORM: a comprehensive ImageJ plug-in for PALM and STORM data analysis and super-resolution imaging. Bioinforma Oxf Engl 30:2389–2390. https://doi.org/10.1093/bioinformatics/btu202
64. Schneider CA, Rasband WS, Eliceiri KW. 2012. NIH Image to ImageJ: 25 years of image analysis. Nat Methods 9:671–675. https://doi.org/10.1038/nmeth.2089
65. Schindelin J, Arganda-Carreras I, Frise E, Kaynig V, Longair M, Pietzsch T, Preibisch S, Rueden C, Saalfeld S, Schmid B, Tinevez J-Y, White DJ, Hartenstein V, Eliceiri K, Tomancak P, Cardona A. 2012. Fiji: an open-source platform for biological-image analysis. Nat Methods 9:676–682. https://doi.org/10.1038/nmeth.2019
66. Nieuwenhuizen RPJ, Lidke KA, Bates M, Puig DL, Grünwald D, Stallinga S, Rieger B. 2013. Measuring image resolution in optical nanoscopy. Nat Methods 10:557–562. https://doi.org/10.1038/nmeth.2448